Title

Fingerprinting triangular-lattice antiferromagnet by excitation gaps

Journal

Physical Review B, 103(18)

ISSN

2469-9950

Authors

Avers, KE
Maksimov, PA
Rosa, PFS
et al.

Publication Date

2021-05-01

DOI

10.1103/physrevb.103.l180406

Peer reviewed

Fingerprinting Triangular-Lattice Antiferromagnet by Excitation Gaps

K. E. Avers,[1,2,3] P. A. Maksimov,[4] P. F. S. Rosa,[1] S. M. Thomas,[1]
J. D. Thompson,[1] W. P. Halperin,[2] R. Movshovich,[1] and A. L. Chernyshev[5]

[1]*Los Alamos National Laboratory, Los Alamos, NM 87545, USA*
[2]*Department of Physics and Astronomy, Northwestern University, Evanston, IL, USA*
[3]*Center for Applied Physics & Superconducting Technologies, Northwestern University, Evanston, IL, USA*
[4]*Bogolyubov Laboratory of Theoretical Physics, Joint Institute for Nuclear Research, Dubna, Moscow region, 141980, Russia*
[5]*Department of Physics and Astronomy, University of California, Irvine, California 92697, USA*

(Dated: April 22, 2021)

$CeCd_3As_3$ is a rare-earth triangular-lattice antiferromagnet with large inter-layer separation. Our field-dependent heat capacity measurements at dilution fridge temperatures allow us to trace the field-evolution of the spin-excitation gaps throughout the antiferromagnetic and paramagnetic regions. The distinct gap evolution places strong constraints on the microscopic pseudo-spin model, which, in return, yields a close *quantitative* description of the gap behavior. This analysis provides crucial insights into the nature of the magnetic state of $CeCd_3As_3$, with a certainty regarding its stripe order and low-energy model parameters that sets a compelling paradigm for exploring and understanding the rapidly growing family of the rare-earth-based triangular-lattice systems.

Rare-earth-based quantum magnets are of great current interest, as they naturally combine the effects of strong spin-orbit coupling (SOC), which entangles magnetic degrees of freedom and orbital orientations [1, 2], with that of the geometric frustration of the lattices bearing a triangular motif, long anticipated as leading to exotic ground states and excitations [3, 4]. A remarkable recent surge in the studies of quantum anisotropic-exchange magnets in general and rare-earth based triangular-lattice (TL) materials in particular is propelled by an avalanche of the newly synthesized compounds [5–22] and theoretical insights into their models [4, 23–28]. Rare-earth materials provide an ideal platform for the search of novel phases as they host short-range and highly anisotropic exchange interactions of their effective spin degrees of freedom due to strong SOC and highly-localized nature of the f-orbitals.

In this Letter, we present low-temperature heat capacity measurements of a Ce-based representative member of this family of materials, $CeCd_3As_3$, in a regime that has not been accessed in the earlier studies [29]. These measurements enable us to construct the magnetic field–temperature (H–T) phase diagram of $CeCd_3As_3$ and determine the field-evolution of the spin-excitation gaps in its spectrum throughout the transition from a frustrated antiferromagnetic (AF) to a paramagnetic (PM) state. We augment these results by a theoretical analysis that yields a close agreement with a distinct field-dependence of the gaps and allows us to unequivocally identify the ground state of $CeCd_3As_3$ as being in a stripe phase. The phenomenological constraints on the key parameters of the microscopic model result in robust certainty regarding the ground state and parameter region of the general phase diagram of the anisotropic-exchange TL systems to which $CeCd_3As_3$ likely belongs. Our approach is expected to enable a better understanding of the rapidly growing family of rare-earth-based TL materials.

Material and Methods.—$CeCd_3As_3$ crystallizes as thin ($\sim$1×1×0.2 mm), plate-like crystals in the hexagonal $P6_3/mmc$ space group in which Ce^{+3} ions form 2D triangular lattices that are widely spaced along the c-axis, as shown in Supplemental Material (SM) [30]. Its low-temperature magnetization is characteristic of an easy-plane anisotropy with a ratio of Lande g-factors $g_{ab}/g_c \sim 5$ [29–31]. Additional experimental details and crystal-field analysis of magnetic susceptibility/magnetization are provided in SM [30]. Here we focus on our study of the specific heat and its theoretical modeling.

H–T phase diagram.—In zero field, $CeCd_3As_3$ orders at T_N=410(20) mK in agreement with a recent report [29] of AF ordering at $T_N \sim 420$ mK. At T_N, only about one quarter of the entropy of the ground state doublet $R\ln 2$ is recovered [30]. The substantial difference between T_N and the ab-plane Curie-Weiss (CW) temperature $\theta_{CW} = -4.5$ K also suggests a large degree of frustration in $CeCd_3As_3$ [32], although with the caveat that the CW temperature can only serve as a crude estimate of the spins' exchange strength in rare-earth materials.

For magnetic fields applied in the ab-plane, T_N increases, reaches its maximum of 500(30) mK near 2 T, and is suppressed at higher fields, see Fig. 1 and Fig. 2(a). Above 3.5 T, at temperatures above the sharp feature that is identified with the magnetic ordering, specific heat also exhibits a shoulder-like anomaly denoted as T_U in Fig. 2(b). In Fig. 1, we highlight the crossover (XO) region between these two features as a shaded area. Both anomalies are suppressed to zero temperature by a magnetic field near 4.7–4.8 T, suggesting a quantum critical point (QCP) within that field range. As is shown in Fig. 1, this region of the phase diagram demonstrates a significant enhancement of the specific heat at a reference low temperature of 100 mK.

Specific heat, T_N and T_U.—Specific heat data for $CeCd_3As_3$ is presented in Fig. 2 for several field and temperature regimes. The data up to 3 T is shown in Fig. 2(a). It demonstrates the non-monotonic T_N field-dependence, characterized by an initial increase followed by a suppression. Such an increase indicates an enhance-

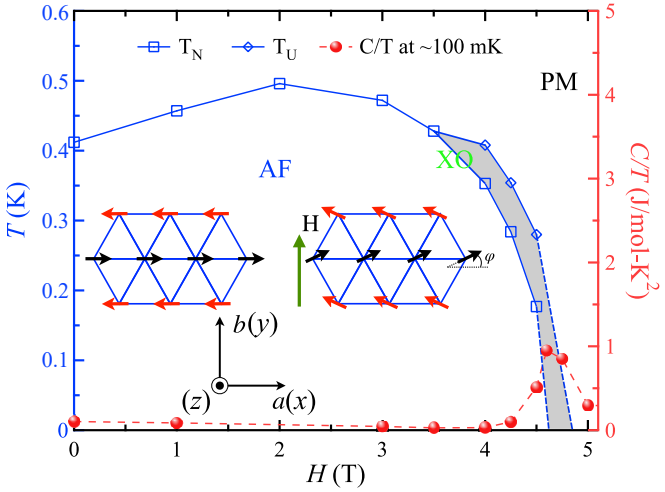

FIG. 1. Open symbols are T_N and T_U vs in-plane field H from the heat capacity data in Figs. 2(a) and (b); closed circles are C/T values at 100 mK, lines are guides to the eye. A crossover (XO) region between T_N and T_U is highlighted. Insert: sketch of the stripe-**x** AF phase in zero and finite field, see text.

ment of the AF order with field and is known to occur in several quantum magnets and their models [33–35], wherein this effect is associated with the field-induced suppression of quantum or thermal spin fluctuations or a reduction of frustration. Given our subsequent analysis of the nature of its magnetic ordered state, we ascribe the increase of T_N in the case of $CeCd_3As_3$ to a field-induced suppression of critical fluctuations related to the phase transition, see SM [30].

As is shown in Fig. 2(b) for the fields 4 T and above, specific heat acquires an additional shoulder-like feature at $T_U > T_N$, giving rise to an XO region between the two temperatures, see also Fig. 1. It appears that the line of T_N transitions continues through 3.5 T with no inflection. Both T_U and T_N decrease towards zero temperature at higher fields, in agreement with the expected suppression of the AF order parameter to zero at a QCP. For the XO region of the phase diagram, we note that while some frustrated TL models consistently have a two-peak structure in their specific heat [36], the second, higher-temperature anomaly at T_U in Fig. 2(b) could also be related to a field-induced high density of states in the magnon spectrum, see Ref. [30].

Specific heat, low-T.—Fig. 2(c) focuses on the low-T heat capacity. As is already indicated in Fig. 1, the behavior of C/T in this temperature range near a presumptive QCP is drastically different from that in other fields regions. It should also be noted that the QCP region is where universal scalings are expected to dictate the T-dependence of all thermodynamic quantities [37].

Fig. 2(c) also displays the specific heat as a function of T for several representative fields away from the QCP region (solid symbols). At $T = 100$ mK, C/T is small up to 4.25 T and is suppressed again in fields greater than 5 T. Moreover, the temperature dependence of C/T in Fig. 2(c) in fields outside of the critical region clearly in-

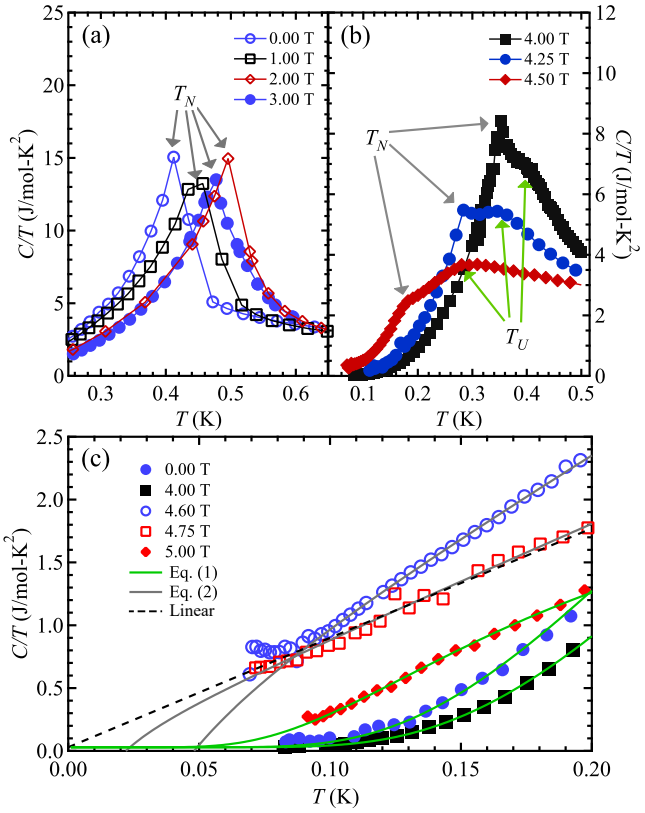

FIG. 2. Specific heat C/T vs T shows: (a) the non-monotonic field-dependence of T_N for $H < 3.5$ T, (b) the emergence of T_U and the XO region for $H > 3.5$ T, lines are guides to the eye, (c) the low-T dependence of C/T away and at the QCP together with the fits from Eqs. (1) and (2) (lines).

dicates activated behavior characteristic of gapped systems, as we elaborate below.

The enhancement in low-T entropy, manifested as a build up of area under the C/T vs T curves, occurs for fields between 4.25 T and 5 T. This results in the large C/T values at 100 mK shown in Fig. 1. The value of C/T at 100 mK is substantially enhanced, reaching a maximum of about 1 J/mol-K^2 at 4.6 T. It is also accompanied by a distinct change in the temperature dependence, shown in Fig. 2(c) for 4.6 T and 4.75 T (open symbols), that is indicative of a power-law in T. The rise in C/T below 80 mK for H=4.6 T is likely due to our calorimeter setup not accurately accounting for longer internal thermal relaxation times in this H–T range.

Low-T asymptotes.—The leading contribution to the heat capacity from a 2D gapped excitation can be obtained by approximating its energy as $\varepsilon_{\mathbf{k}} \approx \Delta + J\mathbf{k}^2$ near the minimum gap Δ and J parametrizing the bandwidth

$$C(T)/T = A\left(x^2 + 2x + 2\right)e^{-x} + \gamma + O\left(e^{-2x}\right), \quad (1)$$

where $x = \Delta/T$, $A \sim 1/J$, and γ is a background Sommerfeld term that we fix at 0.029 J/mol-K^2 for all fits to account for the residual electronic component [30]. The 2D activated behavior of Eq. (1) fits very well all C/T data up to 200 mK for fields away from the QCP region, as is demonstrated in Fig. 2(c), see also Ref. [30].

Since the fit in Eq. (1) is controlled by a single parameter Δ, this analysis allows us to accurately trace the field-dependence of the lowest excitation gap in $CeCd_3As_3$.

For systems with continuous spin symmetries, field-induced PM to AF transition is of the Bose-Einstein condensation type [37, 38]. In our case, because SOC leaves no continuous symmetries intact, this transition is of a different universality class, characterized by the closing of the excitation spectrum gap in a relativistic manner, $\varepsilon_{\mathbf{k}} \approx \sqrt{\Delta^2 + J^2\mathbf{k}^2}$ [37]. This implies an acoustic mode at the QCP, $\varepsilon_{\mathbf{k}} \propto |\mathbf{k}|$ (dynamical exponent $z=1$), leading to a universal 2D scaling, $C(T) \propto T^2$, at the transition field. The gap closure also explains the peak in C/T vs field in Figs. 1 and 2(c) near the QCP.

At 4.75 T, $CeCd_3As_3$ appears to be close to the QCP, as is indicated by the linear fit of C/T (dashed line) in Fig. 2(c), which is indicative of gapless excitations. For small gaps, we obtain a modified scaling

$$C(T)/T \approx A\,T\left(1 - x^2/\alpha\right) + \gamma\,, \qquad (2)$$

with $\alpha = 12\zeta(3)$, valid down to $T \sim \Delta/2$ [30]. Eq. (2) provides an excellent fit to the 4.6 T and 4.75 T data sets in Fig. 2(c) (solid lines), putting an upper bound on Δ at 4.75 T of $\lesssim$90 mK and of $\approx$200 mK at 4.6 T.

Gaps and other phenomenologies.—The spectrum gap Δ, extracted from the specific heat data using Eqs. (1) and (2), is shown in Fig. 3 vs H. The semi-log scale is to accommodate $\Delta \approx 6$ K at 9 T deep in the PM phase. Most of the results in Fig. 3 use $C(T)$ data from the temperature window 0–200 mK and are checked for stability by varying this fitting range. Error bars combine internal quality of the fits with such variations, see SM [30].

The zero-field gap of 0.91(9) K is compatible with the CW temperature [29, 30] and shows no sign of closing below the QCP, implying that the AF phase of $CeCd_3As_3$ evolves continuously with H. Magnetization data corroborate this assertion [30] showing no traces of the plateau-like phase transitions emblematic of TL magnets [39, 40].

The field-dependence of Δ demonstrates an essential feature. It shows a gradual increase to about 1.1 K at 3.5 T followed by an abrupt closing upon approaching the critical field. This non-monotonic behavior is an important distinguishing hallmark that allows us to unambiguously identify the ordered state of $CeCd_3As_3$.

Model.—For Kramers ions in layered compounds, crystal field effects (CEF) lead to an energy splitting of the local Hilbert space of the rare-earth ion magnetic moment into a series of doublets [41]. At temperatures much lower than the crystal field splitting, the lowest Kramers doublets, naturally parametrized as effective pseudo-spins $S = \frac{1}{2}$, are responsible for the dominant magnetic properties of insulating materials. Because of the entanglement with the orbital orientations that are tied to the lattice due to CEF, the pairwise interactions of these pseudo-spins *a priori* retain no spin-rotational symmetries [4, 23]. Instead, it is the discrete symmetries of the lattice that restrict possible forms of the bond-dependent

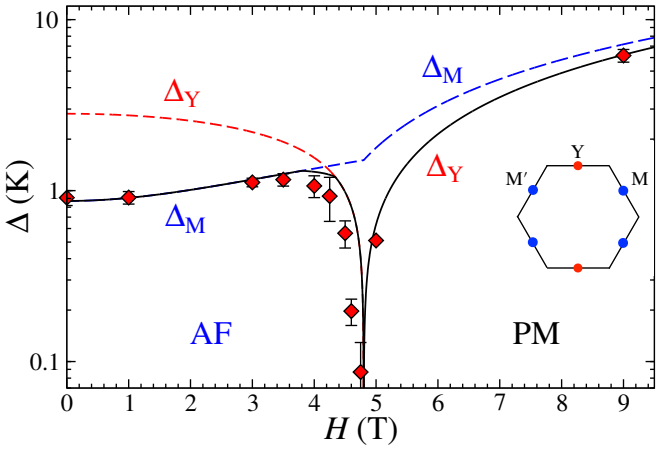

FIG. 3. Δ vs H obtained using Eqs. (1) and (2) (symbols). The excitation spectrum gaps at the ordering vector Y ($\Delta_{\rm Y}$) and complimentary M point ($\Delta_{\rm M}$) for the parameters of the model (3) discussed in text. Inset: Brillouin zone with the Y and M points for the stripe phase in Fig. 1.

interactions. Together with the localized nature of f-orbitals that limits the ranges of interactions, these symmetries lead to generic Hamiltonians that are expected to adequately describe *all* rare-earth-based Kramers compounds on a given lattice [24].

For a layered TL structure, the relevant point-group symmetry operations allow four terms in the Hamiltonian that can be separated into bond-independent, H^{XXZ}, and bond-dependent, H^{bd}, parts, see Ref. [27],

$$\begin{aligned}
\mathcal{H} &= \sum_{\langle ij\rangle}\left(H^{XXZ}_{\langle ij\rangle} + H^{bd}_{\langle ij\rangle}\right) + \sum_{\langle ij\rangle_2} H^{XXZ}_{\langle ij\rangle}, \\
H^{XXZ}_{\langle ij\rangle_m} &= J_m\left(S^x_i S^x_j + S^y_i S^y_j + \bar{\Delta} S^z_i S^z_j\right) \qquad (3)\\
H^{bd}_{\langle ij\rangle} &= 2J_{\pm\pm}\Big[\left(S^x_i S^x_j - S^y_i S^y_j\right)\tilde{c}_\alpha - \left(S^x_i S^y_j + S^y_i S^x_j\right)\tilde{s}_\alpha\Big] \\
&\quad + J_{z\pm}\Big[\left(S^y_i S^z_j + S^z_i S^y_j\right)\tilde{c}_\alpha - \left(S^x_i S^z_j + S^z_i S^x_j\right)\tilde{s}_\alpha\Big],
\end{aligned}$$

where $\tilde{c}(\tilde{s})_\alpha = \cos(\sin)\tilde{\varphi}_\alpha$, $\tilde{\varphi}_\alpha$ are angles of the primitive vectors with the x axis, $\tilde{\varphi}_\alpha = \{0, 2\pi/3, -2\pi/3\}$, and $\{x, y, z\}$ are the crystallographic axes, see Fig. 1. The bond-independent exchange constants J_m are J_1 and J_2 for the first- and second-neighbor couplings, respectively. Following prior works [26, 42], we use a minimal extension of the model by the J_2 term with the same XXZ anisotropy $\bar{\Delta}$. In an external field, Zeeman coupling

$$\mathcal{H}_Z = -\mu_B \sum_i \Big[g_{ab}\left(H_x S^x_i + H_y S^y_i\right) + g_c H_z S^z_i\Big] \qquad (4)$$

contains anisotropic g-factors of the pseudo-spins that reflect the build-up of the ground-state doublets from the states of the **J**-multiplet of the rare-earth ions by a combined effect of SOC and CEF. The in-plane g-factor is uniform because of the TL three-fold symmetry [43].

Phase identification.—As the model (3) has no spin-rotational symmetries [23, 26], one expects gapped excitations throughout its phase diagram, but accidental degeneracies render most of the phases, such as

well-known 120° phase and the nearby incommensurate phases, nearly gapless [27, 44]. Of the remaining phases, the $CeCd_3As_3$ phenomenology of a single-phase field-evolution and a sizable spin-excitation gap strongly suggests so-called stripe phases as prime contenders for its ground state. In a stripe phase, ferromagnetic rows of spins arrange themselves in an AF fashion, see inset of Fig. 1. In particular, as we argue in this work, the non-monotonic field-dependence of the gap is a hallmark of the stripe phases. An alternative scenario of the strongly Ising limit leads to phases and transitions [40, 45] that are incompatible with the phenomenology of $CeCd_3As_3$, see SM [30] for more detail.

Most importantly, the field-evolution of the spin-excitation spectrum in the stripe phase, at the QCP, and in the spin-polarized PM phase are all in accord with our results for $CeCd_3As_3$. Specifically, the spectrum minima in zero field are *not* associated with the ordering vector (identified as a Y-point in Fig. 3), but are complementary to it (M-points in the Brillouin zone). This feature is characteristic of the systems with significant frustrating bond-dependent interactions [27, 28]. In an applied field, it is the gap at the ordering vector that must close, leading to a rather abrupt switch of the minimal gap between the M and Y-points, as is demonstrated in Fig. 3 for a choice of parameters in model (3) discussed next.

Model parameters.—Assuming a stripe ground state, we obtain the field-evolution of spin excitations for model (3) in the AF and PM phases. There are two empirical quantities that provide strong constraints on the model parameters: the value of the critical field, H_s, which we take as 4.8 T, allowing for an ambiguity in the QCP for $CeCd_3As_3$, and the zero-field gap, Δ_0, taken as 0.87 K to account for an uncertainty of the fit. Qualitatively, with $g_{ab} \approx 2$ known from the in-plane magnetization data [30, 31], the empirical value of H_s strongly binds the cumulative exchange term, $J_1 + J_2$, while Δ_0 restricts the $J_{\pm\pm}$ anisotropic-exchange term, see SM [30] for details.

We find the second anisotropic-exchange term, $J_{z\pm}$, to have a minor effect on the spectrum [27] and neglect it in our consideration. This mild simplifying assumption leaves two types of stripe states, stripe-**x** and stripe-**y**, which correspond to spins along and perpendicular to the bonds of the lattice, respectively, indistinguishable up to a change of the sign of the $J_{\pm\pm}$-term and a switch of the field direction from $H \parallel b$ to $H \parallel a$. Because experiments in $CeCd_3As_3$ have not discriminated between the in-plane field directions, we take a minimal-model approach [30], by assuming $J_{\pm\pm} < 0$, which corresponds to stripe-**x** with H along the b-direction shown in Fig. 1.

We have found that the excitation gaps are virtually insensitive to the value of the XXZ anisotropy $\bar{\Delta}$, which is loosely bound in the range 0.5–1.5 by the out-of-plane saturation field, extrapolated from $M(H)$ data [30]. The situation is similar with the ratio J_2/J_1, which does not affect observables at the fixed total $J_1 + J_2$. Thus, by taking XXZ anisotropy $\bar{\Delta} = 1$ and making an *ad hoc* choice of $J_2/J_1 = 0.1$ for the highly localized f-orbitals, for the empirical H_s and Δ_0 we obtain $J_1 \approx 1.19$ K and $J_{\pm\pm} \approx -0.31$ K [30]. With these model parameters, we derive the field-evolution of the gaps shown in Fig. 3.

Our results show a gradual increase of the magnon gap energy $\Delta_{\rm M}$ vs field at the complementary M-point and concurrent decrease of the spin-excitation energy $\Delta_{\rm Y}$ at the ordering vector [30] which inevitably takes the role of the global minimum of the spectrum upon approaching the QCP, all in close accord with the data in Fig. 3. At the QCP, the asymptotic form of the spectrum adheres to the expected relativistic form. Above the QCP, the gap at the Y point reopens, with the spectrum experiencing a roughly uniform, Zeeman-like shift vs H. Remarkably, the high-field value of the gap at 9 T deep in the PM phase is also closely matched by the same model with no additional free parameters.

Summary.—In summary, we have demonstrated that a combination of insights from the low-temperature specific heat data and theoretical modeling provide a comprehensive description of the ground state and excitations in a TL rare-earth anisotropic-exchange magnet, paving the way to a deeper understanding of a broad class of materials. The phenomenological constraints on the general microscopic model have resulted in a precise identification of $CeCd_3As_3$ magnetic ground state as a stripe phase and with a remarkable level of certainty regarding the part of the phase diagram where it belongs.

This study is of immediate relevance to $KCeS_2$ [46], $KErSe_2$ [47], and isostructural $CeCd_3P_3$ [48], where some of the same phenomenology has been observed. Future studies by thermodynamic and spectroscopic methods, such as low-T magnetization, nuclear and electronic magnetic resonance, neutron and x-ray magnetic dichroism scattering, are expected to provide further insights into the nature of the crossover region in the H–T phase diagram and into the role of structural disorder in the static and dynamic properties of these materials. With more theoretical input, they should yield more systematic constraints on the model and elucidate the role of different terms in unusual magnetic states and excitations of anisotropic-exchange magnets.

ACKNOWLEDGMENTS

Acknowledgments—Low-temperature specific heat, magnetization, and electrical resistivity measurements were supported by the U.S. Department of Energy, Office of Science, National Quantum Information Science Research Centers, Quantum Science Center (QSC). Sample synthesis and crystal structure determination were supported by the Los Alamos Laboratory Directed Research and Development project 20190076ER. Scanning electron microscope and energy dispersive X-ray measurements were performed at the Center for Integrated Nanotechnologies, an Office of Science User Facility operated for the U.S. Department of Energy (DOE) Office of Science. Support is acknowledged from

the Northwestern-Fermilab Center for Applied Physics and Superconducting Technologies and by the U.S. Department of Energy, Office of Science, Office of Workforce Development for Teachers and Scientists, Office of Science Graduate Student Research (SCGSR) program (K. E. A). The SCGSR program is administered by the Oak Ridge Institute for Science and Education for the DOE under contract number DE-SC0014664. The work of A. L. C. was supported by the U.S. Department of Energy, Office of Science, Basic Energy Sciences under Awards No. DE-FG02-04ER46174 and DE-SC0021221. P. A. M. acknowledges support from JINR Grant for young scientists 21-302-03. A. L. C. would like to thank Kavli Institute for Theoretical Physics (KITP) where this work was advanced. KITP is supported by the National Science Foundation under Grant No. NSF PHY-1748958.

[1] W. Witczak-Krempa, G. Chen, Y. B. Kim, and L. Balents, Correlated Quantum Phenomena in the Strong Spin-Orbit Regime, Annu. Rev. Cond. Mat. Phys. **5**, 57 (2014).

[2] L. Balents, Spin Liquids in Frustrated Magnets, Nature **464**, 199 (2010).

[3] P. Anderson, Resonating Valence Bonds: A New Kind of Insulator, Mater. Res. Bull. **8**, 153 (1973).

[4] Y. Li, P. Gegenwart, and A. A. Tsirlin, Spin Liquids in Geometrically Perfect Triangular Antiferromagnets, J. Phys. Condens. Matter **32**, 224004 (2020).

[5] Y. Li, H. Liao, Z. Shang, S. Li, F. Jin, L. Ling, L. Zhang, Y. Zou, L. Pi, Z. Yang, J. Wang, Z. Wu, and Q. Zhang, Gapless Quantum Spin Liquid Ground State in the Two-Dimensional Spin-$\frac{1}{2}$ Triangular Antiferromagnet $YbMgGaO_4$, Sci. Rep. **5**, 1 (2015).

[6] M. B. Sanders, F. A. Cevallos, and R. J. Cava, Magnetism in the $KBaRE(BO_3)_2$ (RE=Sm, Eu, Gd, Tb, Dy, Ho, Er, Tm, Yb, Lu) Series: Materials with a Triangular Rare Earth Lattice, Mater. Res Express **4**, 036102 (2017).

[7] M. Bordelon, E. Kenney, C. Liu, T. Hogan, L. Posthuma, M. Kavand, Y. Lu, M. Sherwin, N. P. Butch, C. Brown, M. J. Graf, L. Balents, and S. D. Wilson, Field-Tunable Quantum Disordered Ground State in the Triangular-Lattice Antiferromagnet $NaYbO_2$, Nature Phys. **15**, 1058 (2019).

[8] M. Baenitz, P. Schlender, J. Sichelschmidt, Y. A. Onykiienko, Z. Zangeneh, K. M. Ranjith, R. Sarkar, L. Hozoi, H. C. Walker, J. C. Orain, H. Yasuoka, J. van den Brink, H. H. Klasuss, D. S. Inosov, and T. Doret, $NaYbS_2$: A planar spin-$\frac{1}{2}$ triangular-tattice magnet and putative spin liquid, Phys. Rev. B **98**, 220409(R) (2018).

[9] J. Sichelschmidt, B. Schmidt, P. Schlender, S. Khim, T. Doert, and M. Baenitz, Effective Spin-$\frac{1}{2}$ Moments on a Yb^{3+} Traingular Lattice: an ESR Study, JPS Conf. Prov. **30**, 011096 (2020).

[10] J. Sichelschmidt, P. Schlender, B. Schmidt, M. Baenitz, and T. Doert, Electron Spin Resonance on the Spin-$\frac{1}{2}$ Triangular Magnet $NaYbS_2$, J. Phys. Condens. Matter **31**, 205601 (2019).

[11] F. A. Cevallos, K. Stolze, T. Kong, and R. J. Cava, Anisotropic Magnetic Properties of the Triangular Plane Lattice Material $TmMgGaO_4$, Mater. Res. Bull. **105**, 154 (2018).

[12] Y. Li, S. Bachus, H. Deng, W. Schmidt, H. Thoma, V. Hutanu, Y. Tokiwa, A. A. Tsirlin, and P. Gegenwart, Partial Up-Up-down Order with the Continuously Distributed Order Parameter in the Triangular Antiferromagnet $TmMgGaO_4$, Phys. Rev. X **10**, 011007 (2020).

[13] W. Liu, Z. Zhang, J. Ji, Y. Liu, J. Li, X. Wang, H. Lei, G. Chen, and Q. Zhang, Rare-Earth Chalcogenides: A Large Family of Triangular Lattice Spin Liquid Candidates, Chin. Phys. Lett. **35**, 117501 (2018).

[14] L. Ding, P. Manuel, S. Bachus, F. Grussler, P. Gegenwart, J. Singleton, R. D. Johnson, H. C. Walker, D. T. Adroja, A. D. Hillier, and A. A. Tsirlin, Gapless Spin-Liquid State in the Structurally Disorder-Free Triangular Antiferromagnet $NaYbO_2$, Phys. Rev. B **100**, 144432 (2019).

[15] K. M. Ranjith, D. Dmytriieva, S. Khim, J. Sichelschmidt, D. Ehlers, H. Yasuoka, J. Wosnitza, A. A. Tsirlin, H. Kuhne, and M. Baenitz, Field-Induced Instability of the Quantum-Spin-Liquid Ground State in the $J_{eff} = \frac{1}{2}$ Triangular-Lattice Compound $NaYbO_2$, Phys. Rev. B **99**, 180401 (2019).

[16] K. M. Ranjith, S. Luther, T. Reimann, B. Schmidt, P. Schlender, J. Sichelschmidt, H. Yasuoka, A. M. Strydom, Y. Skourski, J. Wosnitza, H. Kuhne, T. Doert, and M. Baenitz, Anisotropic Field-Induced Ordering in the Triangular-Lattice Quantum Spin Liquid $NaYbSe_2$, Phys. Rev. B **100**, 224417 (2019).

[17] J. Xing, L. D. Sanjeewa, J. Kim, G. R. Stewart, A. Podlesnyak, and A. S. Sefat, Field-Induced Magnetic Transition and Spin Fluctuation in Quantum Spin Liquid Candidate $CsYbSe_2$, Phys. Rev. B **100**, 220407(R) (2019).

[18] J. Xing, L. D. Sanjeewa, J. Kim, W. R. Meier, A. F. May, Q. Zheng, R. Custelcean, G. R. Stewart, and A. S. Sefat, Synthesis, Magnetization and Heat Capacity of Triangular Lattice Materials $NaErSe_2$ and $KErSe_2$, Phys. Rev. Mater. **3**, 114413 (2019).

[19] J. Xing, L. D. Sanjeewa, J. Kim, G. R. Stewart, M.-H. Du, F. A. Reboredo, R. Custelcean, and A. S. Sefat, Crystal Synthesis and Frustrated Magnetism in Triangular Lattice $CsRESe_2$ (RE=La-Lu):Quantum Spin-Liquid Candidates, ACS Mater. Lett. **2**, 71 (2020).

[20] A. Scheie, V. O. Garlea, L. D. Sanjeewa, J. Xing, and A. S. Sefat, Crystal Field Hamiltonian and Anisotropy in $KErSe_2$ and $CsErSe_2$, Phys. Rev. B **101**, 144432 (2020).

[21] J. Ma et al., Spin-Orbit-Coupled Triangular-Lattice Spin Liquid in Rare-Earth Chalcogenides (2020), arXiv:2002.09224.

[22] N. Kabeya, T. Sakamoto, K. Hara, Y. Hara, S. Nakamura, K. Katoh, and A. Ochiai, Competing Exchange Interactions in Lanthanide Triangular Lattice Compounds $LnZn_3P_3$ (Ln=La-Nd, Sm, Gd), J. Phys. Soc. Japan **89**, 074707 (2020).

[23] Y. D. Li, X. Wang, and G. Chen, Anisotropic Spin Model

of Strong Spin-Orbit-Coupled Triangular Antiferromagnets, Phys. Rev. B **94**, 035107 (2016).
[24] J. G. Rau and M. J. P. Gingras, Frustration and Anisotropic Exchange in Ytterbium Magnets with Edge-Shared Octahedra, Phys. Rev. B **98**, 054408 (2018).
[25] Z. Zhu, P. Maksimov, S. White, and A. Chernyshev, Disorder-Induced Mimicry of a Spin Liquid in $YbMgGaO_4$, Phys. Rev. Lett. **119**, 157201 (2017).
[26] Z. Zhu, P. Maksimov, S. White, and A. Chernyshev, Topography of Spin Liquids on a Traingular Lattice, Phys. Rev. Lett. **120**, 207203 (2018).
[27] P. A. Maksimov, Z. Zhu, S. R. White, and A. L. Chernyshev, Anisotropic-Exchange Magnets on a Triangular Lattice: Spin Waves, Accidental Degeneracies, and Dual Spin Liquids, Phys. Rev. X **9**, 021017 (2019).
[28] P. A. Maksimov and A. L. Chernyshev, Rethinking α-$RuCl_3$, Phys. Rev. Research **2**, 033011 (2020).
[29] S. R. Dunsiger, J. Lee, J. E. Sonier, and E. D. Mun, Long-Range Magnetic Order in the Anisotropic Triangular Lattice System $CeCd_3As_3$, Phys. Rev. B **102**, 064405 (2020).
[30] (2021), Supplemental Material at http://link.aps.org/supplemental/XXX contains technical details, additional magnetization, susceptibility and resistivity results, phase diagram of model (3), consideration of different phases related to $CeCd_3As_3$ phenomenology, details of the spin-wave theory results for the spectrum in the AF stripe and PM phases and for Neel temperature, derivations of the asymptotic expressions for the specific heat in Eqs. (1) and (2), and model parameter considerations. It also includes Refs. [49–57].
[31] J. Banda, B. K. Rai, H. Rosner, E. Morosan, C. Geibel, and M. Brando, Crystalline Electric Field of Ce in Trigonal Symmetry: $CeIr_3Ge_7$ as a Model Case, Phys. Rev. B **98**, 195120 (2018).
[32] Y. Q. Liu, S. J. Zhang, J. L. Lv, S. K. Su, T. Dong, G. Chen, and N. L. Wang, Revealing a Triangular Lattice Ising Antiferromagnet in a Single-Crystal $CeCd_3As_3$ (2016), arXiv:1612.03720.
[33] R. Ishii, S. Tanaka, K. Onuma, Y. Nambu, M. Tokunaga, T. Sakakibara, N. Kawashima, Y. Maeno, C. Broholm, and D. P. Gautreaux, Successive Phase Transitions and Phase Diagrams for the Quasi-Two-Dimensional Easy-Axis Triangular Antiferromagnet $Rb_4Mn(MoO_4)_3$, Europhysics Lett. **94**, 17001 (2011).
[34] M. Gvozdikova, P.-E. Melchy, and M.-E. Zhitomirsky, Magnetic Phase Diagrams of Classical Triangular and Kagome Antiferromagnets, J. Phys.: Condens. Matter **23**, 164209 (2011).
[35] P. Sengupta, C. D. Batista, R. D. McDonald, S. Cox, J. Singleton, L. Huang, T. P. Papageorgiou, O. Ignatchik, T. Herrmannsdorfer, J. L. Manson, J. A. Schlueter, K. A. Funk, and J. Wosnitza, Nonmonotonic Field Dependence of the Néel Temperature in the Quasi-Two-Dimensional Magnet $[Cu(HF_2)(pyz)_2]BF_4$, Phys. Rev. B **79**, 060409(R) (2009).
[36] B. Schmidt and P. Thalmeier, Frustrated Two Dimensional Quantum Magnets, Phys. Rep. **703**, 1 (2017).
[37] V. Zapf, M. Jamie, and C. D. Batista, Bose-Einstein Condensation in Quantum Magnets, Rev. Mod. Phys. **86**, 563 (2014).
[38] E. G. Batyev and L. S. Braginskii, Antiferrormagnet in a Strong Magnetic Field: Analogy with Bose Gas, Sov. Phys. JETP **60**, 781 (1984).
[39] O. A. Starykh, Unusual Ordered Phases of Highly Frustrated Magnets: a Review, Rep. Prog. Phys. **78**, 052502 (2015).
[40] L. Seabra and N. Shannon, Competition Between Supersolid Phases and Magnetization Plateaus in the Frustrated Easy-Axis Antiferromagnet on a Triangular Lattice, Phys. Rev. B **83**, 134412 (2011).
[41] M. T. Hutchings, Point-Charge Calculations of Energy Levels of Magentic Ions in Crystalline Electric Fields, Solid State Phys. **16**, 227 (1964).
[42] J. A. M. Paddison, M. Daum, Z. Dun, G. Ehlers, Y. Liu, M. B. Stone, H. Zhou, and M. Mourigal, Continuous Excitations of the Triangular-Lattice Quantum Spin Liquid $YbMgGaO_4$, Nature Phys. **13**, 117 (2017).
[43] Y. Li, G. Chen, W. Tong, L. Pi, J. Liu, Z. Yang, X. Wang, and Q. Zhang, Rare-Earth Triangular Lattice Spin Liquid: A Single-Crystal Study of $YbMgGaO_4$, Phys. Rev. Lett. **115**, 167203 (2015).
[44] J. G. Rau, P. A. McClarty, and R. Moessner, Pseudo-Goldstone Gaps and Order-by-Quantum-Disorder in Frustrated Magnets, Phys. Rev. Lett. **121**, 237201 (2018).
[45] S. Miyashita, Magnetic Properties of Ising-Like Heisenberg Antiferromagnets on the Triangular Lattice, J. Phys. Soc. Japan **55**, 3605 (1986).
[46] G. Bastien, B. Rubrecht, E. Haeussler, P. Schlender, Z. Zangeneh, S. Avdoshenko, R. Sarkar, A. Alfonsov, S. Luther, Y. A. Onykiienko, H. C. Walker, H. Kuhne, V. Grinenko, Z. Guguchia, V. Kataev, H.-H. Klauss, L. Hozoi, J. van den Brink, D. S. Inosov, B. Buchner, A. U. B. Wolter, and T. Doert, Long-Range Magnetic Order in the $\tilde{S} = 1/2$ Triangular Lattice Antiferromagnet $KCeS_2$, SciPost Phys. **9**, 041 (2020).
[47] J. Xing, K. M. Taddei, L. D. Sanjeewa, R. S. Fishman, M. Daum, M. Mourigal, C. dela Cruz, and A. S. Sefat, Stripe Antiferromagnetic Ground State of Ideal Triangular Lattice $KErSe_2$, Phys. Rev. B **103**, 144413 (2021).
[48] J. Lee, A. Rabus, N. Lee-Hone, D. Broun, and E. Mun, The Two-Dimensional Metallic Triangular Lattice Antiferromagnet $CeCd_3P_3$, Phys. Rev. B **99**, 245159 (2019).
[49] E. Gopal, Specific Heats at Low Temperatures, The International Cryogenics Monograph Series (Springer US, 1966).
[50] Y. T. Fan, W. H. Lee, and Y. Y. Chen, Antiferromagnetic Spin Wave in Ce_2PdGe_6, Phys. Rev. B **69**, 132401 (2004).
[51] W. P. Halperin, F. Rasmussen, C. Archie, and R. Richardson, Properties of Melting ^{3}He: Specific Heat, Entropy, Latent Heat, and Temperature, J. Low Temp. Phys. **31**, 617 (1978).
[52] P. Pagliuso, D. Garcia, E. Miranda, E. Granado, R. Serrano, C. Giles, J. Duque, R. Urbano, C. Rettori, J. Thompson, M. Hundley, and J. Sarro, Evolution of the Magnetic Properties and Magnetic Structures Along the R_mMIn_{3m+2} (R=Ce, Nd, Gd, Tb; M=Rh, Ir; and m=1,2) Series of Intermetallic Compounds, J. Appl. Phys. **99**, 08P703 (2006).
[53] S. S. Stoyko and A. Mar, Ternary Rare-Earth Arsenides $REZn_3As_3$(RE=La-Nd, Sm) and $RECd_3As_3$(RE=La-Pr), Inorg. Chem. **50**, 11152 (2011).
[54] Y. D. Li, Y. Shen, Y. Li, J. Zhao, and G. Chen, Effect of Spin-Orbit Coupling on the Effective-Spin Correlation in $YbMgGaO_4$, Phys. Rev. B **97**, 125105 (2018).

[55] E. V. Komleva, V. Y. Irkhin, I. V. Solovyev, M. I. Katsnelson, and S. V. Streltsov, Unconventional Magnetism and Electronic State in Frustrated Layered System $PdCrO_2$, Phys. Rev. B **102**, 174438 (2020).

[56] S. Higuchi, Y. Noshima, N. Shirakawa, M. Tsubota, and J. Kitagawa, Optical, Transport and Magnetic Properties of New Compound $CeCd_3P_3$, Mat. Res. Exp. **3**, 056101 (2016).

[57] W. M. Steinhardt, Z. Shi, A. Samarakoon, S. Dissanayake, D. Graf, Y. Liu, W. Zhu, C. Marjerrison, C. D. Batista, and S. Haravifard, Contraining the Parameter Space of a Quantum Spin Liquid Candidate in Applied Field with Iterative Optimization (2020), arXiv:1902.07825.

Fingerprinting Triangular-Lattice Antiferromagnet by Excitation Gaps: Supplemental Material

K. E. Avers,[1,2,3] P. A. Maksimov,[4] P. F. S. Rosa,[1] S. M. Thomas,[1]
J. D. Thompson,[1] W. P. Halperin,[2] R. Movshovich,[1] and A. L. Chernyshev[5]

[1]*Los Alamos National Laboratory, Los Alamos, NM 87545, USA*
[2]*Department of Physics and Astronomy, Northwestern University, Evanston, IL, USA*
[3]*Center for Applied Physics & Superconducting Technologies, Northwestern University, Evanston, IL, USA*
[4]*Bogolyubov Laboratory of Theoretical Physics, Joint Institute for Nuclear Research, Dubna, Moscow region, 141980, Russia*
[5]*Department of Physics and Astronomy, University of California, Irvine, California 92697, USA*

(Dated: April 22, 2021)

CONTENTS

I. Experimental details and other data 1
A. Experimental methods 1
B. Crystal structure 2
C. Magnetization and susceptibility 2
1. Crystal electric field levels 3
D. Heat capacity 3
1. Zero field entropy 3
2. Entropy vs field 4
3. High-temperature specific heat 4
4. Spin-excitation gaps from the low-T specific heat 5
E. Electrical resistivity 6
F. Comparison with $CeCd_3P_3$ 6

II. Theoretical model 7

III. Phases 7

IV. Case of $CeCd_3As_3$ 8

V. Phase identification 9

VI. Stripe phase 10
A. A minimal model 10
B. Stripe domains 10
C. Saturation fields and magnetization 11
D. Spin-wave theory 12
E. Gaps 13
F. Parameter sets 13
G. Gap vs field results 14
H. Polarized phase 14
I. Ising phase gaps 16

VII. Néel temperature 16

VIII. Specific heat and various asymptotes 17
A. Gapped spectrum 17
B. Gapless spectrum at the critical point 17
C. Other anomalies in the specific heat 18

References 18

I. EXPERIMENTAL DETAILS AND OTHER DATA

A. Experimental methods

Bulk single crystals of $CeCd_3As_3$ were grown by chemical vapor transport using iodine as a transport agent and recipe described in Ref. [1, 2]. Polycrystalline $CeCd_3As_3$ was first synthesized by solid state reaction. A stoichiometric mixture of Ce, Cd and As pieces was sealed in a quartz tube under partial Ar atmosphere and heated to 800 °C for one week. The resulting polycrystal was sealed in a quartz tube with iodine and placed in the hot end of a zone furnace. The other end of the tube was held at 700 °C where single crystal platelets of typical size 1 mm were obtained. The crystallographic structure was verified by single-crystal diffraction at room temperature, using Mo radiation in a Bruker D8 Venture diffractometer, and was consistent with previous results [1, 2]. The stoichiometry of the single crystals was confirmed by elemental analysis using energy-dispersive x-ray spectroscopy in a commercial scanning electron microscope.

Heat capacity measurements were performed in a dilution refrigerator down to 70 mK using the heat pulse technique. A RuO thermometer was attached directly to one side of the sample with GE varnish. The other side of the sample was attached to a sapphire substrate with a heater on the opposite side of the substrate. The weak thermal link wire was silver painted directly to the sample. No evidence for multiple timescale relaxation behavior was observed indicating good thermal contact between the sample, RuO thermometer, heater, and sapphire substrate, as well as fast internal relaxation time of the sample. No subtraction of electron nor phonon heat capacity contributions from the sample, heater, sapphire, or thermometer were performed because the magnetic heat capacity of $CeCd_3As_3$ is vastly dominant in the temperature range of interest in this work. It is estimated that the magnetic degrees of freedom contribute more than 99 percent of the entropy change from 0 K to 2 K. The calorimeter was weakly thermally linked to a copper temperature regulation block, and a temperature stabilized Lakeshore automatic bridge with active feedback PID system was employed. The sample RuO thermometer was previously calibrated in magnetic field up to 9 T.

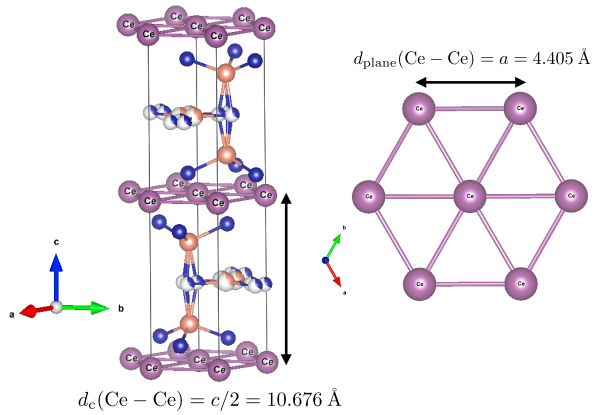

FIG. 1. (left) Crystal structure of $CeCd_3As_3$, which crystallizes in space group #194 ($P6_3/mmc$). Orange and blue circles represent Cd and As atoms, respectively. (right) The two-dimensional triangular arrangement of the magnetic Ce^{3+} atoms.

Measurements of resistivity vs temperature were performed in zero field down to 95 mK using a Quantum Design physical property measurement system with an adiabatic demagnetization refrigeration attachment. The sample was taken from the same batch as the sample used for heat capacity measurements. It was glued to a copper cold finger using GE varnish with cigarette paper providing electrical insulation. Four 25 micron platinum wires were spot welded to the sample, and resistivity was measured by the 4-wire method. Multiple excitation currents were applied to ensure Joule heating was not significant.

Magnetization measurements were performed using a commercial Quantum Design MPMS SQUID-based magnetometer.

B. Crystal structure

$CeCd_3As_3$ crystallizes in the $PrZn_3As_3$-type structure (space group $P6_3/mmc$) with lattice parameters a=b=4.4051 Å and c=21.3511 Å, as shown in Fig. 1. Magnetic rare-earth Ce^{+3} ions form planes of 2D triangular lattices that are separated from each other by layers of As and Cd atoms with an aspect ratio of inter-plane to intra-plane Ce spacing of approximately 2.4. There is only one cerium site in this structure, but both Cd and As atoms have two sites, one of which is only 1/3 occupied. Though this partial occupancy does not distort the Ce triangular structure directly, the role of disorder in this material remains poorly understood.

C. Magnetization and susceptibility

The higher temperature investigation of thermodynamic properties provide important clues into the nature of magnetism in $CeCd_3As_3$. The magnetic susceptibility (χ) vs temperature (T) is presented in Fig. 2(a). The data were taken in an applied field of 1 T both along the c-axis (blue squares), and within the ab-plane (red circles). A simple Curie-Weiss law does not describe the

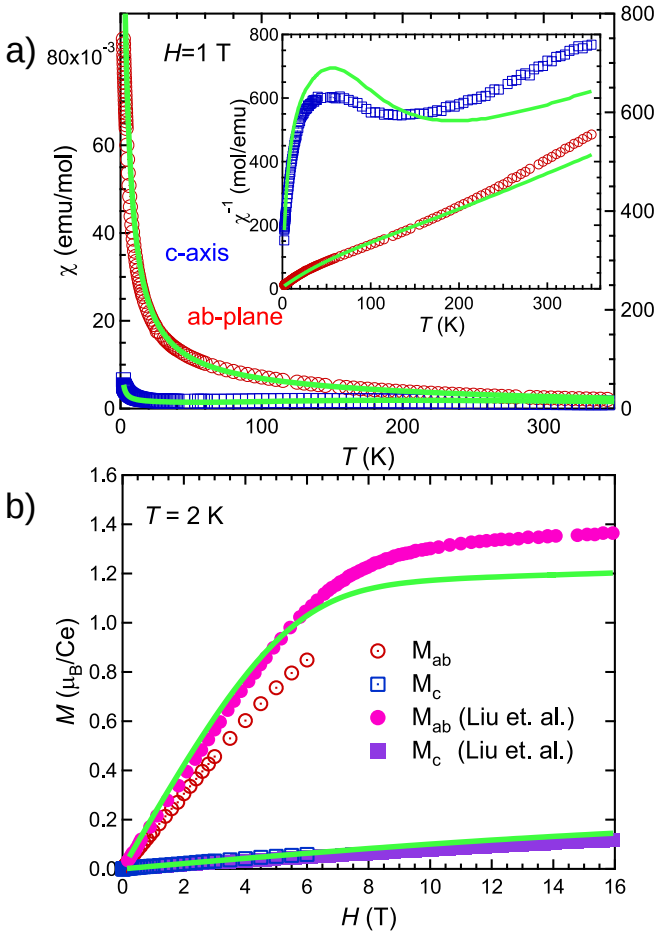

FIG. 2. a) Susceptibility ($\chi = \frac{M}{H}$) vs temperature (T) taken with H=1 T along the c-axis, and within the ab-plane with the inverse susceptibility (χ^{-1}) in the insert. The infection points in χ^{-1} are due to the influence of excited doublets of the Ce moment. The light green curves are fits to data as described in the text. b) Magnetization (M) vs field (H) at T=2 K to H=6 T along the c-axis and within the ab plane alongside the data of Liu et. al. [2]. The light green curve is calculated by integrating the low temperature susceptibility. Even though the fit only reaches 1.2 μ_b/Ce it is relatively good agreement.

experimental results. $\chi(T)^{-1}$, shown in the insert, is visibly non-monotonic for the field along the c-axis, with a local minimum near 140 K. Careful inspection of the susceptibility for the field in the ab-plane reveals inflection points in its temperature behavior as well. Fig. 2(b) presents magnetization (M) vs field (H) results at 2 K for magnetic field up to 6 T applied along the c-axis (open blue squares) and within the ab-plane (open red circles). We also plot data at 1.9 K up to 16 T extracted from Ref. [2] (filled circles and squares). The strong magnetization anisotropy of roughly 10 between the (easy) ab-plane and the (hard) c-axis was initially taken as evidence for strong antiferromagnetic interactions of Ising-like spins aligned along the c-axis [2]; however, inspection of the temperature dependent susceptibility shows that this may be an inaccurate description of the physics of this system.

As recognized in Ref. [3], the high-temperature non-monotonic behavior in χ vs T can be accounted for by a non-interacting model involving the Zeeman term and the trigonal crystalline electric field (CEF) Hamiltonian $\mathcal{H}_{\rm CEF} = B_2^0 O_2^0 + B_4^0 O_4^0 + B_4^4 O_4^3$, in which B_i^n are the CEF parameters and O_i^n are the Stevens equivalent operators [3]. The trigonal $\mathcal{H}_{\rm CEF}$ splits the $j = \frac{5}{2}$ sixfold degenerate state of Ce^{3+} into three doublets, two of which are a mixture of $|m_j = \pm 5/2\rangle$ and $|\pm 1/2\rangle$ states. In an attempt to capture the low-temperature magnetization of $CeCd_3As_3$, here we also include the spin Hamiltonian $\mathcal{H}_{\rm spin} = \tilde{J}_1 \sum \mathbf{j}_i \cdot \mathbf{j}_j$, in which $\tilde{J}_1 > 0$ represents AF interactions between nearest neighbors, and $\mathbf{j}_i$ is the total angular momentum operator on site i. Following Ref. [4], we employ a mean-field approximation, which allows the spin Hamiltonian to be written simply as $z\tilde{J}_1 \sum_i \mathbf{j}_i \cdot \langle \mathbf{j} \rangle$, with $z = 6$ being the number of nearest neighbors. Our results give a CEF doublet hierarchy with the lowest energy doublet dominated by the $|\pm 1/2\rangle$ states. This ground state doublet gives rise to an g-factor anisotropy that causes the moments to lie in the ab-plane at low temperatures, which explains the aforementioned strong magnetization anisotropy. The two excited doublets that would allow the magnetic moment to point out of the ab-plane are separated from the ground state by 372 K, and 545 K, respectively, and hence are not populated at the low temperatures where the AF phase emerges. They may be responsible for the observed inflection points in $\chi(T)$.

Considering a CEF plus nearest-neighbor interaction Hamiltonian does not describe the data well, but including additional mean field antiferromagnetic interactions ($\tilde{J}_1 = 0.8$ K and $\tilde{J}_2 = 0.6$ K) produces a reasonable, although not unique, fit shown as light green curves in Fig 2(a) with CEF parameters ($B_2^0 = 11.5$ K, $B_4^0 = -1.4$ K, and $B_4^3 = 12$ K) in good agreement with Ref. [3]. The need for two mean field antiferromagnetic interactions is indicative of additional frustration, not present in the nearest-neighbor-only model. The fits reproduce the inflection points in $\chi(T)^{-1}$, although suffer in accuracy for the c-axis direction. This mismatch is likely because $|\chi(T)|$ is quite small along that direction leading to increased measurement error. This demonstrates that the inflections are due to the CEF doublet hierarchy, and not impurities as suggested in [2]. The inclusion of these interactions does indeed allow an accurate calculation of the M vs H behavior matching Liu et. al. quite well for low fields. The saturation of magnetization and its magnitude at 6 T for the field in the ab-plane is slightly mismatched, but still qualitatively reproduces the effect. The saturation magnetization of $\sim 1.2\ \mu_B$/Ce in the ab-plane is consistent with the lowest energy Ce^{+3} doublet and the results in Ref. [3]. One possible source of the discrepancy of our data with that of Ref. [2] is in the mass normalization due to small crystal sizes. This is also consistent with the observation that $C(T)$ reported in that work is larger than ours. We have carefully verified the accuracy of such mass determination on our end.

Despite the measured susceptibility not being described by a Curie-Weiss law for the entire temperature range, it is still possible to locally fit the data to a Curie-Weiss law at low temperature in order to extract the effective Weiss temperature. This will provide an average measure and sign of the interaction strength. We performed Curie-Weiss fits to the χ for $T < 10$ K for c-axis, and for $T < 25$ K for the ab-plane, where the system is in the ground state doublet and far away from any inflection points. We obtain effective Weiss temperatures (Θ) of -5.1 K and -4.5 K, respectively, which are consistent with previous results [2].

1. *Crystal electric field levels*

The crystal electric field levels of the $j = \frac{5}{2}$ Ce^{+3} are doubly degenerate due to Kramer's theorem for half-integer spin systems. The levels, $|n = 0, 1, 2\rangle$ in increasing order of energy as expressed as the eigen functions of $\hat{j}_z$ are listed in Table I. Our results are also similar to $KErSe_2$ and $CsErSe_2$ in which the CEF levels were measured by powder neutron diffraction [5].

$\|0\rangle = 0.32\|\pm 5/2\rangle + 0.95\|\mp 1/2\rangle$	E=0 K
$\|1\rangle = 0.95\|\pm 5/2\rangle + 0.32\|\mp 1/2\rangle$	E=372 K
$\|2\rangle = \|\pm 3/2\rangle$	E=545 K

TABLE I. The crystal electric field eigenfunctions, and energy level relative to the ground state of the Ce^{+3} obtained from the model as described in the main text. Take note of the $\pm$, and $\mp$ that indicate each level is doubly degenerate in zero field.

D. Heat capacity

1. *Zero field entropy*

The effects of magnetic frustration become evident in the heat capacity of $CeCd_3As_3$. The zero-field heat capacity (C/T) and the associated change in entropy (ΔS) as a function of temperature are plotted in Fig. 3 with a photograph of the sample in the inset. C/T data display a sharp lambda peak at $T_N = 412$ mK indicating a phase transition from the high-temperature paramagnetic state to a low-temperature AF state. We also observe the effect of frustration in the entropy change, ΔS, plotted as the cyan curve in Fig. 3. By taking the integral of C/T, one obtains ΔS from 0 K to 2.2 K to be nearly 80% of Rln2, whereas the change in entropy from 0 K to T_N for $CeCd_3As_3$ is only approximately 25% of Rln2, which is a signature of magnetic frustration, see also Ref. [6]. The Rln(2) limit is likely reached at about 8 K, in agreement with Ref. [6], which, however, did not accumulate all low-T entropy from below $\sim$0.4K.

We note that for an unfrustrated system, one should recover at least 50% Rln2 of entropy from $T = 0$ to T_N, depending on the symmetry of the system, e.g. Heisenberg, Ising, or XY [7]. This is the case in Ce_2PdGe_6 [8], or the nuclear antiferromagnet ^{3}He [9].

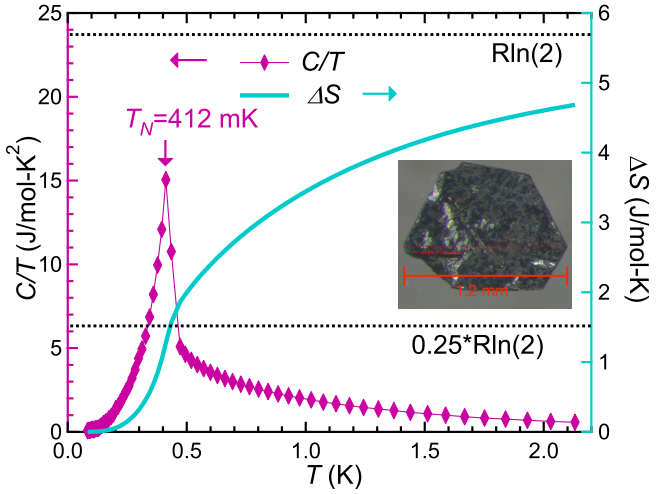

FIG. 3. Zero-field specific heat and integrated entropy data as a function of temperature. At the antiferromagnetic phase transition with T_N=412 mK, the entropy is only 25% of Rln2. A photograph of the sample is in the inset.

2. *Entropy vs field*

The entropy change vs field for relevant temperature integration ranges is shown in Fig. 4. The total entropy change from 0 K to 2.2 K monotonically decreases as a function of field. In contrast, the entropy change from 0 K to T_N is nearly constant. Once the T_U feature described in the main text emerges in the C/T, the entropy change rapidly decreases as field increases. The red and purple lines are linear fits to the 0 K to T_U and 0 K to T_N points, respectively. The entropy change trends towards zero at $\sim$ 4.8 T and $\sim$ 4.6 T for T_U and T_N, respectively. The linear fits interpolate to $\sim$ Rln(2) and $\sim$80 % Rln(2) at zero field for T_U and T_N, respectively.

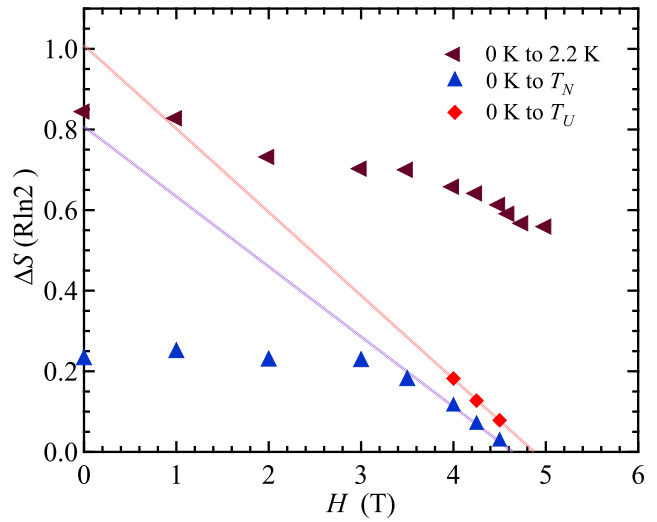

FIG. 4. Entropy change as a function of field for various intervals of temperature integration.

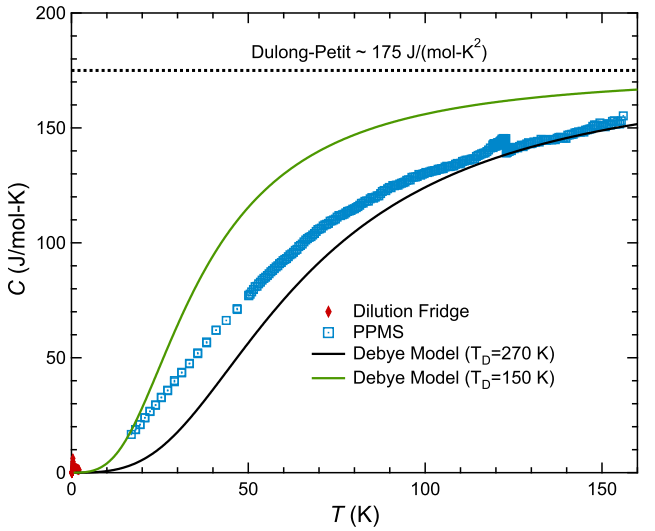

FIG. 5. Specific heat from the low- and high-T measurements. Debye-model results for two representative Debye temperatures, Dulong-Petit limit is also indicated.

3. *High-temperature specific heat*

In Fig. 5, we present our specific heat data for $CeCd_3As_3$ for the temperatures up to 160 K. In agreement with the prior work on this and related compounds, see Refs. [6, 10], the one-parameter Debye model fails to provide adequate description of $C(T)$ at intermediate temperatures, which indicates possible nearly dispersionless phonon modes [7]. However, as this model is expected to provide an adequate estimate of the low-T and high-T limit of the lattice contribution to $C(T)$, such an exposition is still instructive.

In Fig. 5, we plot the calculated Debye $C(T)$ for two Debye temperatures, T_D, of 150 K and 270 K, which can be argued to provide reasonable bounds on the overall phonon energy scale. The expected upper limit of the lattice contribution at $T \gg T_D$ is also indicated. Then a simple estimate using the low-temperature Debye approximation ($\sim T^3$) with a reasonable T_D of 220 K gives the lattice contribution at 2 K, the upper limit of most of our $C(T)$ dilution fridge measurements, as $C_{ph}(T = 2\,\mathrm{K}) \approx 0.01$ J/mole-K. This is, indeed, several orders of magnitude lower than the magnetic contribution reported in this work, as is mentioned above.

While our data in Fig. 5 is generally in a good agreement with the recent work of Ref. [6], there is a small anomaly in it at $T_s \sim 125$ K, somewhat lower than a similar feature reported in [6]. This feature is indicative of a structural transition. There is also an affiliated anomaly in resistivity, discussed below. However, there are no discernible indications of this transition in the magnetic susceptibility. While this is certainly not conclusive and a careful study of whether this transition can cause any direct changes to the magnetic Ce-planes is called for, this observation contributes to the expectation that the magnetism of the rare-earth f-orbitals is not significantly affected by this weak anomaly.

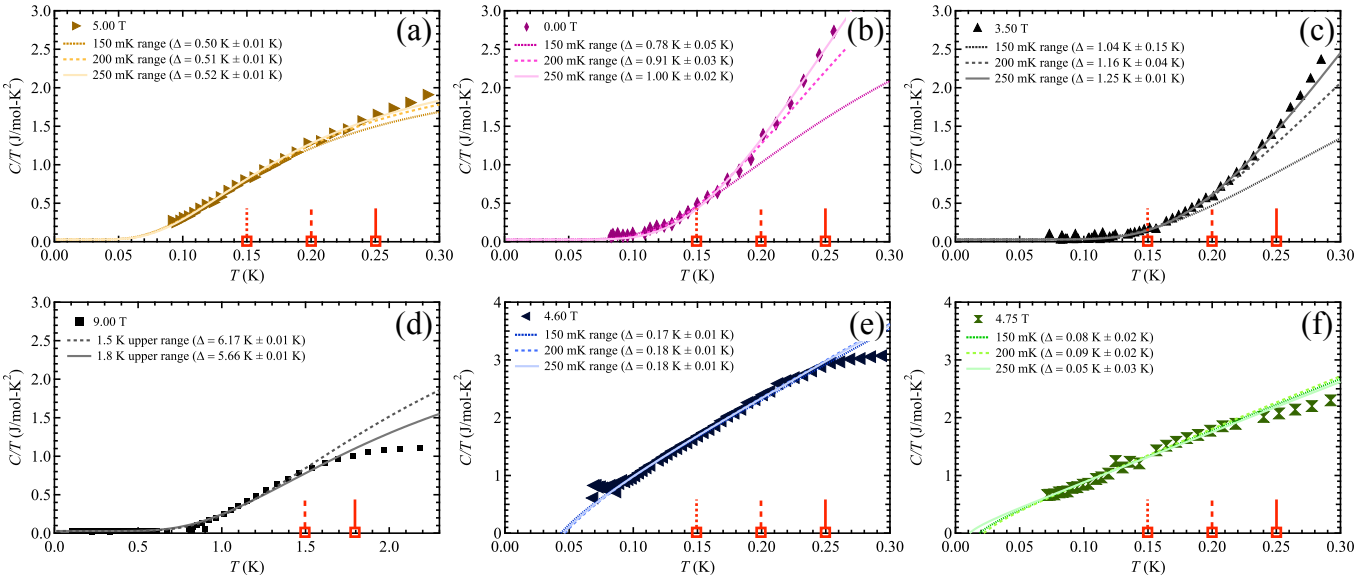

FIG. 6. C/T vs T for selected field values and their fits using asymptotic expressions for the gapped spectra in Sec. VIII [Eqs. (1) and (2) of the main text] for several fitting ranges. Fields 5 T and 9 T, (a) and (d), are for the PM phase, 4.6 T and 4.75 T, (e) and (f), are from the QCP region, 0 T and 3.5 T, (b) and (c), are from the AF phase. Extracted values of Δ and their "intrinsic" errors for each fitting range are listed; upper limits of the ranges are highlighted by riser bars on the T-axis. The lower T-limit for fitting is 0 K for all fits except the 4.6 T data in which we exclude the tail below 90 mK due to thermal equilibrium concerns, the upper limits are 1.5 K and 1.8 K for (d), and 150 mK, 200 mK, and 250 mK for the rest, with the dotted, dashed, and solid lines showing corresponding fits.

4. *Spin-excitation gaps from the low-T specific heat*

Here we use theoretical asymptotic expressions for the spectral gaps obtained in Sec. VIII (Eqs. (1) and (2) of the main text) and demonstrate the robustness of their extracted values with respect to the temperature range.

Our Fig. 6 explicates the details of extracting spectral gap values Δ from the $C(T)$ data. It shows the results for C/T vs T for the field values from the paramagnetic phase, 5 T and 9 T, Fig. 6(a) and (d), from the QCP region, 4.6 T and 4.75 T, Fig. 6(e) and (f), and for the two representative fields, $H = 0$ T and 3.5 T, from the AF ordered phase, Fig. 6(b) and (c), respectively. Each panel lists the extracted value of Δ for each of the chosen temperature fitting range, with the upper limit of the latter also highlighted by the vertical riser bars on the T-axis. It also shows the variance of Δ for that temperature fitting range that characterizes the quality of each fit, which will be referred to as "intrinsic" error. The lower T-limit for fitting is 0 K for all fits except the 4.6 T data in which we exclude the tail below 90 mK due to thermal equilibrium concerns. The upper T-limits, with an exception of the 9 T data in Fig. 6(d), are 150 mK, 200 mK, and 250 mK, with the dotted, dashed, and solid lines showing corresponding fits. For the 9 T data in Fig. 6(d), the upper limits for the fitting ranges are 1.5 K and 1.8 K, dashed and solid lines, respectively. The gap values Δ with their "intrinsic" error bars extracted from each fit are summarized in Fig. 7.

Several comments are in order. The 5 T data, Fig. 6(a), yield $\Delta \approx 0.51(1)$ K essentially independently of the fitting range. This is because in the PM phase and for Δ much smaller than the spin-excitation bandwidth, $C(T)$ is expected to be dominated by the population of the lowest-gap excitation and, thus, is well-described by Eq. (21) [Eq. (1) of the main text]. The second set of data from the PM phase, 9 T in Fig. 6(d), exhibit more variation because the gap in this case is at least the same value as the bandwidth and also possibly because the T-range is larger than the exchange energies.

The resultant gap values are also very stable for the fields from the QCP region, 4.6 T and 4.75 T, Figs. 6(e) and (f), described by the small-gap asymptotic expression (25) [Eq. (2) of the main text], largely for the same reasons as the 5 T results. There is a bit more bias for the 4.75 T set, but this is because the gap is smaller than the lowest temperature for which the data is available.

In the AF phase, 0 T and 3.5 T, Figs. 6(b) and (c), the gap is large ($\sim$1 K). It is clear from Figs. 6(b) and (c) that this makes the lowest shown T-range not representative, because its 150 mK cut-off limits the exponential tail to a small subset of the data that is also a subject of more significant intrinsic variance, especially in case of 3.5 T data where the gap is about 25% higher than in zero field. Thus, while we still show their respective Δ values in the summary plot in Fig. 7 for completeness, we disregard the 150 mK-range results from our analysis for the strongly gapped data sets.

One can see that the 200 mK and 250 mK-range results in Figs. 6(b) and (c) are significantly more consistent. We refrain, however, from the further increase of the fitting ranges in the case of the AF-phase data.

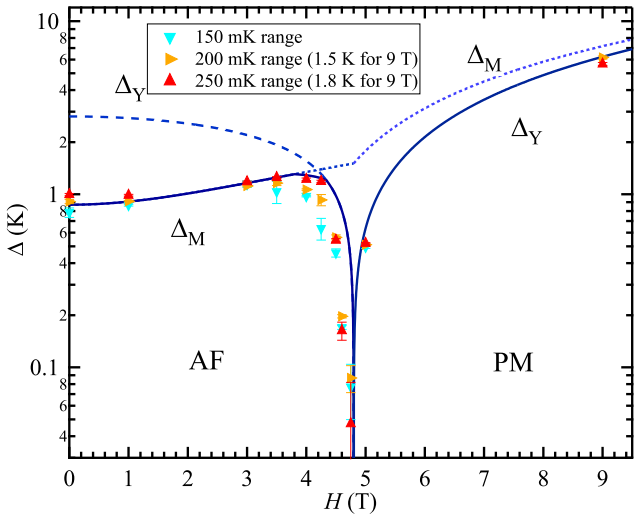

FIG. 7. Same as Fig. 3 of the main text with the data for gap values Δ and their intrinsic error bars extracted from each fit as in Fig. 6.

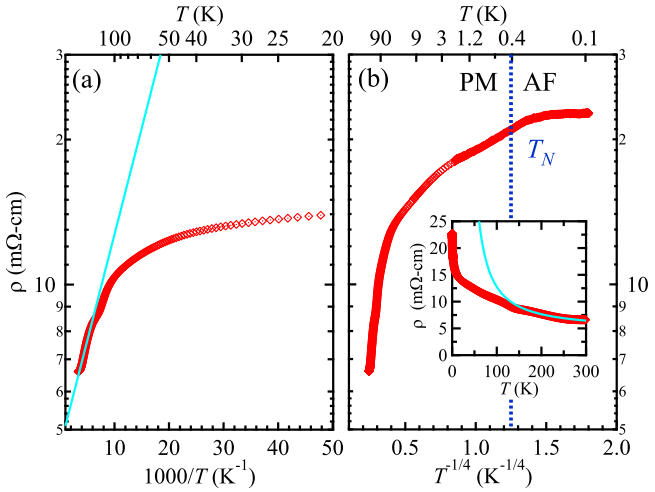

FIG. 8. Electrical resistivity of $CeCd_3As_3$ as a function of temperature. (a) $\log(\rho)$ vs $1000/T$, (b) $\log(\rho)$ vs $T^{-1/4}$, with inset showing ρ vs T. Activated behavior in (a), $\rho = \rho_0 e^{E_g/2T}$ with the fit of $E_g \approx 200$ K, and variable range hoping $\rho \sim e^{(T_0/T)^{1/4}}$ in (b) are suggested. Dashed line is the zero field T_N of the PM-AF transition.

This is because their resulting fit may be biased by the critical fluctuations of the order parameter due to ordering at $T_N \sim 500$ mK, which are unaccounted for by the theory in Eq. (21) [Eq. (1) of the main text]. Instead, we introduce generous estimates on the error bars as the geometric average of the intrinsic variance and the difference of the gap values of the two fitting ranges of 200 mK and 250 mK (1.5 K and 1.8 K for 9 T set). As one can see from Fig. 3 of the main text and from Fig. 21, the resultant errors are still rather small for most of the data.

E. Electrical resistivity

The temperature dependence of electrical resistivity $\rho(T)$ of $CeCd_3As_3$ is presented in Fig. 8. It shows a semiconducting behavior at most temperatures with room-temperature ρ approximately 6.6 $m\Omega$-cm, suggesting low carrier concentration. Although no satisfactory fit range for a single gap semiconductor could be found, the activated Arrhenius fit $\sim e^{E_g/2T}$ of the high-temperature tail yields a gap of $E_g \approx 200$ K (20 meV). However, the situation seems similar to the case of $CeCd_3P_3$, where electrical transport suggested a similarly small activation energy ~ 40 meV, while the direct spectroscopic energy gap was found to be significantly larger, ~ 750 meV, see Ref. [11]. This suggests that the entire family of these materials are indirect band-gap semiconductors and also raises an issue of impurity dopants shifting chemical potential away from the gap. In that context, we note that the resistivity of $CeCd_3As_3$ reported in Ref. [6] is significantly more metallic.

A small dip centered at about 130 K can be observed in Fig. 8(a) in agreement with Ref. [6] and our $C(T)$ results in Fig. 5. A similar anomaly in ρ is observed in $CeCd_3P_3$ and non-magnetic $LaCd_3P_3$ [10] ruling out a magnetic origin. It is likely related to either a subtle change in phonon modes unique to the crystal structure these compounds share or a structural transition.

A $\log(\rho)$ vs $T^{-1/4}$ is shown in Fig. 8(b) with the dashed line indicating the location of the zero field T_N=412 mK PM-AF transition. The lack of any feature in $\rho(T)$ at T_N suggests an extremely weak coupling between charge carries and the magnetic Ce^{+3} ion. The residual resistivity at $T \to 0$ is approximately 23 $m\Omega$-cm. The somewhat linear $\log(\rho)$ vs $T^{-1/4}$ behavior between 2.0 K and 0.3 K suggests that variable range hoping, $\sim e^{(T_0/T)^{1/4}}$, may be playing a role at the lowest temperatures, but again the lack of any sizable fit range makes conclusions on the trap energy T_0 difficult. Multiple excitation currents were attempted, and no Joule heating effect could be observed.

F. Comparison with $CeCd_3P_3$

Finally, we compare our results to those of isostructural $CeCd_3P_3$, which has been synthesized recently in single crystal form [10] by the same group that reported the AF transition in $CeCd_3As_3$ [6]. First, the magnetic susceptibility of $CeCd_3P_3$ is qualitatively and near quantitatively indistinguishable from both our and their results on $CeCd_3As_3$, which suggests nearly identical local CEF environments. Second, $CeCd_3P_3$ orders antiferromagnetically at $T_N = 410$ mK at zero field, and the transition also increases to 430 mK under a 1.5 T easy-plane field, although it is important to emphasize that this field induced increase in T_N for Ce triangular lattices can depend sensitively on precise field direction within the ab-plane as shown in the case of $KCeS_2$ [12]. The authors were unable to measure heat capacity below 370 mK so no comparison of the residual heat capacity,

the emergence of any crossover region, nor the extraction of the spin-wave gap could be done, although such a measurement would be worthwhile. In both compounds they obverse a momentary field induced decrease of T_N for fields below 0.05 T. This is very likely to be domain selection since planer stripe magnetic structures in triangular lattices have three degenerate domains in zero field. There are some discrepancies that could play a role in elucidating the behavior of these systems. The $CeCd_3As_3$ single crystals they made exhibit the same field induced increase of T_N we observed, however their $CeCd_3As_3$ made by flux growth demonstrate electrically conductive behavior whereas ours made by chemical vapor transport are semiconducting (see Fig. 8). However, the very low carrier density of their samples suggests that both compounds likely sit close to a metal-insulator transition. It is self-evident at this point that exact nature of electrical conductivity in these systems is very sensitive to minor details of how they are grown and will require further investigation. The lack of any noticeable difference between our results in terms of heat capacity, magnetization, and susceptibility demonstrates that the charge carries or lack thereof have minimal impact on the magnetic degrees of freedom in these compounds. There are also other closely related lanthanide compounds that deserve scrutiny [13].

II. THEORETICAL MODEL

For a typical layered triangular-lattice structure, the relevant point-group symmetry operations are the C_3 (120°) rotation around the z axis, C_2 (180°) rotation around each bond, site inversion symmetry $\mathcal{I}$, and two translations, $\mathcal{T}_1$ and $\mathcal{T}_2$ along $\boldsymbol{\delta}_1$ and $\boldsymbol{\delta}_2$, respectively [14], see Fig. 9. These symmetries allow four terms in the nearest-neighbor Hamiltonian that can be separated into bond-independent (XXZ) and bond-dependent parts,

$$\begin{aligned}\mathcal{H} &= \sum_{\langle ij\rangle}\left(H^{\bar{\Delta}}_{\langle ij\rangle}+H^{bd}_{\langle ij\rangle}\right)+\sum_{\langle ij\rangle_2}H^{\bar{\Delta}}_{\langle ij\rangle},\\ H^{\bar{\Delta}}_{\langle ij\rangle_m} &= J_m\left(S^x_iS^x_j+S^y_iS^y_j+\bar{\Delta}S^z_iS^z_j\right) \qquad (1)\\ H^{bd}_{\langle ij\rangle} &= 2J_{\pm\pm}\Big[\left(S^x_iS^x_j-S^y_iS^y_j\right)\tilde{c}_\alpha-\left(S^x_iS^y_j+S^y_iS^x_j\right)\tilde{s}_\alpha\Big]\\ &\quad+J_{z\pm}\Big[\left(S^y_iS^z_j+S^z_iS^y_j\right)\tilde{c}_\alpha-\left(S^x_iS^z_j+S^z_iS^x_j\right)\tilde{s}_\alpha\Big],\end{aligned}$$

where $\tilde{c}(\tilde{s})_\alpha=\cos(\sin)\tilde{\varphi}_\alpha$, the bond angles $\tilde{\varphi}_\alpha$ are that of the primitive vectors $\boldsymbol{\delta}_\alpha$ with the x axis, $\tilde{\varphi}_\alpha=\{0,2\pi/3,-2\pi/3\}$, and spin projections are in crystallographic axes that are tied to the lattice, see Fig. 9. The bond-independent exchange constants J_m are J_1 and J_2 for the nearest- and second-nearest-neighbor couplings, respectively. Following previous considerations [15, 16], we use a minimal generalization of the nearest-neighbor model by augmenting it with the second-nearest-neighbor XXZ term with the same anisotropy parameter $\bar{\Delta}$.

In an external field, the standard Zeeman coupling

$$\mathcal{H}_Z=-\mu_B\sum_i\Big[g_{ab}\Big(H_xS_x+H_yS_y\Big)+g_zH_zS_z\Big], \qquad (2)$$

contain anisotropic g-factors of the pseudo-spins that reflect the build-up of the ground-state doublets from the states of the original **J**-multiplet of the rare-earth ions due to a combined effect of spin-orbit coupling and CEF. The in-plane g-factor is uniform because of the three-fold symmetry of the lattice [17].

III. PHASES

Fig. 10 shows a section of the classical $J_{\pm\pm}$–$J_{z\pm}$–J_2 3D phase diagram of the model (1) for a representative choice of $\bar{\Delta}=1$ and antiferromagnetic J_1. All couplings are in units of J_1 and the Hamiltonian is invariant under $J_{z\pm}\to-J_{z\pm}$ [18]. It is obtained by the energy minimization for the commensurate single-**Q** states and, thus, ignores more complicated multiple-**Q** states that occur near some of the phase boundaries as discussed in Ref. [18]. Since they are unimportant for our present consideration we ignore them as well. This phase diagram is essentially the same for the other values of the easy-plane, or "XY-like" $0\le\bar{\Delta}\le1$, aside from the 120° phase extending to somewhat larger values of $J_{z\pm}$ [16, 18].

As is discussed in Refs. [16, 18], the 120° phase is favored by the XXZ part of the Hamiltonian while the stripe phases are favored by the bond-dependent $J_{\pm\pm}$ and $J_{z\pm}$ as well as by the J_2 term. The stripe phases differ by the mutual orientation of spins and bonds. In the stripe-**x** phase, favored by the negative $J_{\pm\pm}$, spins are fully in plane and along one of the bonds. In the stripe-**yz** phase, spins are perpendicular to one of the bonds and are tilted out of plane for the non-zero $J_{z\pm}$. There is an obvious three-fold degeneracy between the stripe states of

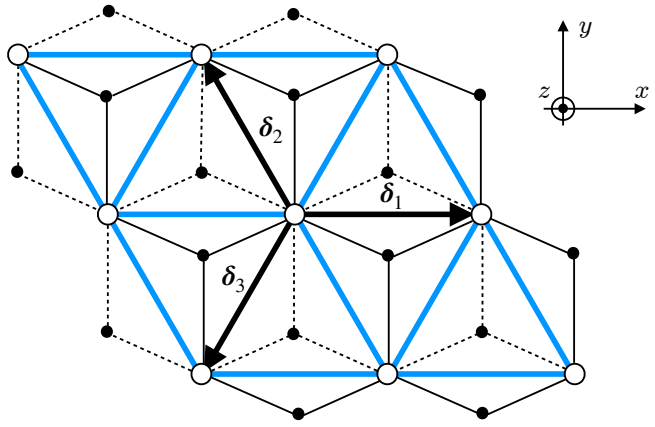

FIG. 9. A sketch of the triangular-lattice layer of magnetic ions (empty circles) embedded in the octahedra of ligands (black dots) with the primitive vectors. Thick (blue) bonds are between magnetic ions and ion-ligand bonds are the thin solid (dashed) lines for above (below) the plane.

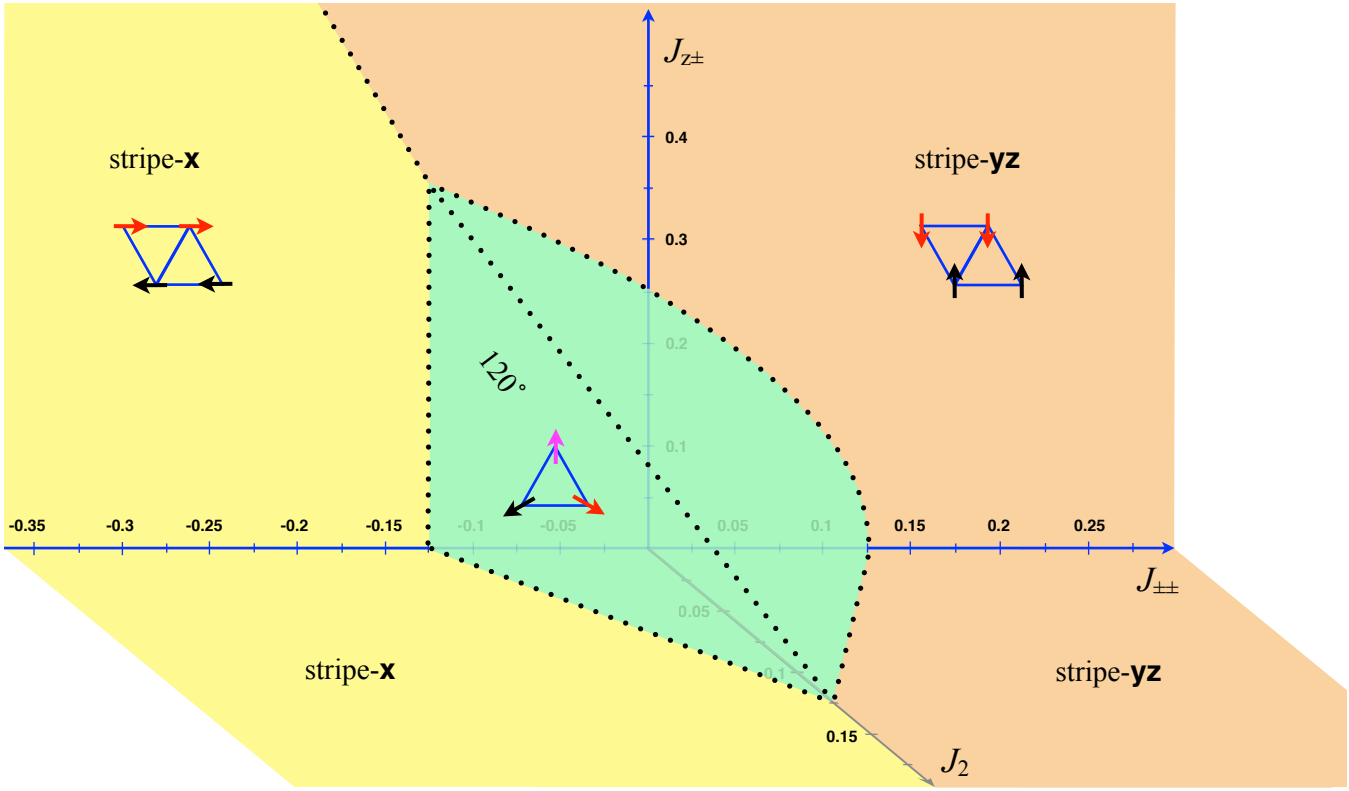

FIG. 10. Classical $J_{\pm\pm}$–$J_{z\pm}$–J_2 phase diagram of the Hamiltonian from the main text with J_2 term for representative $\bar{\Delta}=1$ obtained by the energy minimization for the commensurate single-**Q** states. All couplings in units of $J_1>0$.

different orientation of the "ferromagnetic" bonds along $\boldsymbol{\delta}_{1,2,3}$.

The key message of Fig. 10 is that there are only three ordered antiferromagnetic phases in the phase diagram of the Hamiltonian for $J_1>0$, with or without the J_2-term. For the "Ising-like" $\bar{\Delta}>1$ and finite $J_{\pm\pm}$ and $J_{z\pm}$, stripe phases survive and continue to occupy much of the parameter space. In this limit, the XXZ and bond-dependent anisotropic terms also compete, resulting in a transition to a different stripe phase with the spin pointing out of the plane along the z axis. The full phase diagram for $\bar{\Delta}>1$ also contains ferrimagnetic "Y" phase in place of the 120° phase [19] and, generally, has a complicated cascade of the field-induced phases [20].

IV. CASE OF $CeCd_3As_3$

The essential empirical facts about $CeCd_3As_3$ are the following. It orders antiferromagnetically at $T_N\approx 0.4$ K. The zero-field specific heat shows activated behavior with a sizable excitation gap $\Delta\approx 1$ K, which is compatible to an estimate of a characteristic superexchange constant that one can infer from the extrapolated Curie-Weiss temperatures ($\Theta_{CW}\sim 4$ K) [2].

The magnetization field-dependence, $M(H)$, shows a monotonic increase for both in-plane and out-of-plane field direction before reaching a saturation with some residual Van Vleck slope. Due to a strong easy-plane magnetic anisotropy [3], the actual saturation in the c-direction is beyond the measured field range, which prevents an accurate determination of the saturation field in that direction. The estimates of the corresponding in-plane and out-of-plane g-factors in (2) give a factor of ~ 5 between them, according to Ref. [3].

Most importantly, although taken above the ordering temperature, magnetization curves in both principal directions show no traces of the plateau-like features or of any other phase transitions that are emblematic of the triangular-lattice magnets [20, 21]. We note that the presence of such plateau-like phases in the field-evolution would have definitely made the 120° part of the phase diagram a prime suspect for the zero-field ground state. This lack of the other field-induced phases is also strongly corroborated by the specific heat field-dependence in the in-plane field, which shows no sign of a closing of the excitation gap before the critical point to the paramagnetic state is reached at $H_s^{ab}\approx 4.6$–4.8 T. Together, these facts strongly suggest that the H–T phase diagram of $CeCd_3As_3$ contains a single magnetically-ordered phase that evolves continuously from the $H=0$ state.

To substantiate this statement, we show the specific heat vs temperature data collapse for the fields $0\le H\lesssim H_s^{ab}$ using the rescaling of the temperature by the gap Δ and an *ad hoc* multiplicative constant α for $C(T)/T$ at different fields, see Fig. 11. The single fit is by the leading

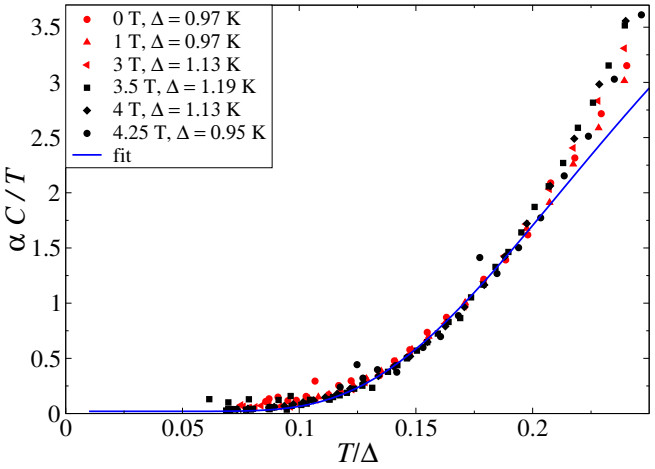

FIG. 11. Data collapse of the $C(T)/T$ vs T data, where $C(T)$ is the specific heat at various fields below H_s^{ab}, with T scaled with the gap Δ and α an *ad hoc* multiplicative constant. Solid line is the fit by the leading term in the 2D activated behavior, Ax^2e^{-x}, where $x=\Delta/T$.

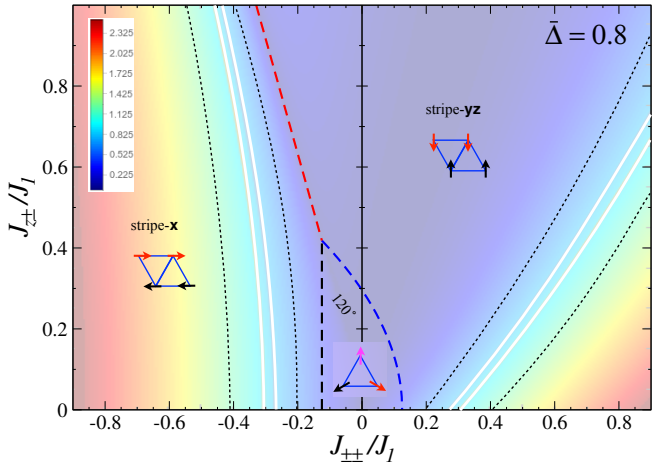

FIG. 12. The 2D $J_{\pm\pm}$–$J_{z\pm}$ phase diagram of the Hamiltonain for $\bar{\Delta}=0.8$, $J_2=0$, all in units of $J_1>0$. Phases are indicated. The intensity plot shows the gap in the spin excitation spectrum. The white solid lines are for $E_{gap}=1$ K for $J_1=1$ K and 1.2 K. The thin black dashed lines are the projections of the outer boundaries of such regions for $\bar{\Delta}=0.5$ and 1.5.

term in the 2D activated behavior, Ax^2e^{-x}, where $x=\Delta/T$, see Sec. VIII for details.

In addition, the field-dependence of the excitation gap extracted from the specific heat data in the main text demonstrates a seemingly more subtle, but an essential feature. It has a noticeable gradual increase by 20%-60% (depending on the fit) from its zero-field value, followed by a rather abrupt closing upon approaching the saturation field. This characteristic behavior turned out to be an important distinguishing hallmark of the field-induced transformations in the magnetic excitation spectrum.

The other significant observations include a characteristic T^2 behavior of the specific heat at the field-induced transition to the paramagnetic state and an initial moderate increase of the Néel temperature vs field that is indicative of a suppression of critical fluctuations.

The key observations that are most important for the subsequent discussion are the gapped ground state and the single-phase character of the ordered phase.

V. PHASE IDENTIFICATION

Because of the combined SOC and CEF effects, the Hamiltonian has no continuous spin-rotational symmetries. Therefore, one should generally expect that *all* its ordered phases host gapped spin excitations. However, the 120° as well as the ferromagnetic states of the classical model exhibit accidental continuous degeneracies [18]. In simple terms, their ground state energies have no contribution from the bond-dependent terms, the orientation of their spin configurations is not fixed beyond the one dictated by the XXZ term, and their spectra are gapless. The gaps open and spin directions get chosen as a result of a quantum order-by-disorder effect, but the gap magnitude is typically a small fraction of the exchange constant [22].

This consideration suggests the stripe phases as strong contenders for the ground state of $CeCd_3As_3$ as they do allow for a sizable spin-excitation gap. The second argument that will be explored later is the simplicity of the field-evolution of the zero-field stripe phases for the most part of the phase diagram. That is, for a stripe state with a considerable gap, spins continuously tilt in a field until reaching a paramagnetic state without encountering intermediate states. Lastly, the spectrum structure in the stripe phases is both peculiar and characteristic of the systems with significant frustrating or bond-dependent interactions. Because of the presence of an accidental degeneracy elsewhere in the phase diagram, the spectral minima are *not* associated with the ordering vector, but are complementary to it [18, 23]. Such a structure has a significant bearing on the field-induced transformations in the magnetic excitation spectrum, which, as we will demonstrate below, are in accord with the experimental observations in $CeCd_3As_3$.

To be quantitative, we would like to demonstrate which regions of the phase diagram of the Hamiltonian $CeCd_3As_3$ can possibly belong. For that, in Fig. 12 we present a 2D version of Fig. 10, the $J_{\pm\pm}$–$J_{z\pm}$ 2D phase diagram of the Hamiltonian for a representative choice of $\bar{\Delta}=0.8$, antiferromagnetic J_1, and $J_2=0$, which shows the same three phases, the 120° and two stripe phases. The underlying intensity plot indicates the size of the gap in the spin excitation spectrum, all in units of J_1. The two solid white lines on each side show the boundaries on the range of $J_{z\pm}$ and $J_{\pm\pm}$ for the choice of the zero-field gap $E_{gap}=1$ K for J_1 varying between 1 K and 1.2 K. The two sets of the thin black dashed lines for positive and negative $J_{\pm\pm}$ show the projections of the outer boundaries of such ranges from the same phase diagrams

but for different values of the XXZ anisotropy, $\bar{\Delta}=0.5$ and $\bar{\Delta}=1.5$, altogether giving a sense of how much the model parameters are constrained by the gap value.

Naively, an alternative scenario for the gapped ground state that may seem to be a much more straightforward option is the Ising-like state. One can expect it to occur for $\bar{\Delta}>1$ in the absence of the bond-dependent terms. First, as was mentioned above, the XXZ and bond-dependent anisotropies may compete in this case, so the stripe phases survive for larger values of $|J_{\pm\pm}|(J_{z\pm})$, leaving our consideration for them intact. Second, for $\bar{\Delta}>1$ the gapless 120° phase converts into a still gapless ferrimagnetic "Y" phase, in which coplanar spins form a deformed "Y" with one spin pointing perpendicular to the plane and two tilted away from it with the mutual angles that differ from 120°, hence the ferrimagnetism [19]. Since the latter is not observed, and the state is also gapless, this phase can be ruled out. The last option from this "Ising domain" is the "stripe-**z**" phase, which occurs at finite J_2 and $\bar{\Delta}>1$ [20] and should be stable for a range of $J_{\pm\pm}$ and $J_{z\pm}$. However, there are two arguments against $CeCd_3As_3$ being in this phase. This phase should exhibit a complicated cascade of the first-order spin-flop-like transitions for the field in the c-direction, see Ref. [20], occurring already in the low enough fields to be be visible in the available finite-temperature $M(H)$ data. No traces of such transitions are seen experimentally. Second, we have also calculated the field-dependence of the gap for a representative set of parameters from this phase, see Sec. VII. As opposed to the stripe-**x**(**yz**) case, the gap behavior vs field is monotonic and is not compatible with the phenomenology of the $CeCd_3As_3$.

VI. STRIPE PHASE

Although the qualitative arguments presented above strongly point toward $CeCd_3As_3$ being in a stripe part of the phase diagram, the model description requires defining, or restricting, of five parameters: two superexchange constants J_1 and J_2, XXZ anisotropy constant $\bar{\Delta}$, and the bond-dependent terms $J_{\pm\pm}$ and $J_{z\pm}$.

A. A minimal model

The ground states and excitation spectra of the stripe phases of the Hamiltonian have been thoroughly considered in zero field [18, 24] and above the saturation field for both the out-of-plane [15, 24] and in-plane [25] field directions. The high-field description is reasonably straightforward and gives clear insights into the role of different terms of the Hamiltonian. In particular, $J_{z\pm}$ does not contribute to the spin-wave spectrum in the polarized phase in the out-of-plane field and the saturation fields H_s in any of the three principal direction, $a(x_0)$, $b(y_0)$, or $c(z_0)$, are also independent of it. For the in-plane field, the $J_{z\pm}$ term does contribute to the spectrum in the polarized state, but its kinematic form is such that it vanishes at all relevant high symmetry points. For the zero-field spectrum, one can also verify that adding a $J_{z\pm}$ term that is comparable to $J_{\pm\pm}$ does not provide any qualitative changes to it [18]. These insights give a significant reason to neglect the $J_{z\pm}$ term from the consideration altogether.

A different qualitative incentive that makes such a move highly desirable is the significantly simpler spin-wave algebra that allows to reduce the rank of the matrices to diagonalize and to derive many expressions in a simple analytical form. We, therefore, will not resist this temptation and, in the following, will put $J_{z\pm}=0$.

The second useful observation [24] is that the linear combination of the superexchange constants J_1 and J_2, in which they enter in the expressions for observables such as saturation fields and energy gaps at high symmetry points as well as into the classical energy of the state, is the same: J_1+J_2. This means that we cannot constrain them independently and they simply define an overall scale of the exchange matrix. Thus, for the following consideration we will simply fix their ratio to a reasonable value that is consistent with the expectations for localized f-orbitals: $J_2/J_1=0.1$. We note that completely neglecting J_2 leads to some additional subtle degeneracies in the spectrum both at zero and at the saturation field that are not generic and are useful to avoid by keeping J_2/J_1 finite.

These choices lead to significant simplifications and leave us with three terms to constrain, J_1, $\bar{\Delta}$, and $J_{\pm\pm}$.

B. Stripe domains

For $J_{z\pm}=0$, spin configurations in the stripe-**x** and stripe-**yz** phases are within the triangular lattice plane (x_0–y_0 or ab plane), aligned with the bond ($J_{\pm\pm}<0$) and perpendicular to it ($J_{\pm\pm}>0$), respectively, see Fig. 13(a) and (e). Their corresponding energies and excitations in zero field are fully symmetric with respect to $J_{\pm\pm}\to -J_{\pm\pm}$ [24]. As was mentioned in Sec. III, there is a three-fold degeneracy of the stripe states in zero field, illustrated in Fig. 13(d), which shows two configurations that are degenerate with the one in Fig. 13(a). The domains of all three states should be present in a material.

There are two principal in-plane field directions, $H\parallel b$ and $H\parallel a$. Theoretically, one of the three domains with the spin configuration that is "most transverse" to the external field will be selected by an infinitesimal field. For instance, for the stripe-**x** phase in the $H\parallel b$ field, the domain in Fig. 13(a) is energetically favored over the domains in Fig. 13(d). In the $H\parallel a$ field, *two* domains in Fig. 13(d) are preferred over the one in Fig. 13(a) and remain degenerate till the saturation field. Experimentally, the domain selection often occurs at some small but finite field because of the lower symmetry of the spin system due to lattice distortions, domain surface energy, disorder

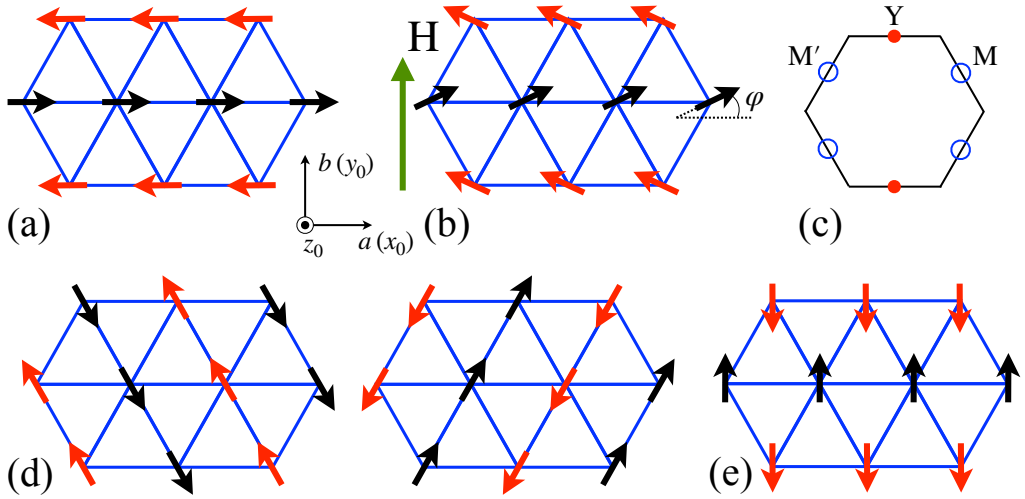

FIG. 13. (a) One of the three domains of the stripe-**x** phase. (b) Spin configuration of that domain in the $H \parallel b$ field. (c) Brillouin zone with the ordering vectors of the stripe phases Y, M, and M′. (d) Two domains of the stripe-**x** phase with the ordering vectors at M and M′. (e) Spin configuration of the stripe-**yz** phase.

pinning, and other real-life complications. The former reason is known to take place in case of α-$RuCl_3$ [23] and a small-field transition has been observed in $CeCd_3P_3$ [10], a material that is related to the present case.

We also note that for $J_{z\pm}=0$, the finite-field consideration of the stripe-**x** and stripe-**yz** phases is fully symmetric under the simultaneous change of sign of $J_{\pm\pm}$ and switching the roles of $H \parallel b$ with $H \parallel a$.

C. Saturation fields and magnetization

To be specific, we will focus on the case of $J_{\pm\pm}<0$ that corresponds to the stripe-**x** phase and select the field direction $H \parallel b$. In this case, the spins cant gradually toward the field as is shown in Fig. 13(b). The corresponding ordering vector for this domain is associated with the Y-point in the Brillouin zone in Fig. 13(c), while the M- and the M′-points are referred to as complementary to it. We also remark that this choice is also the simplest from the analytical point of view as the canting angle in Fig. 13(b) is the same for all the spins. For comparison, the choice of $H \parallel a$ for the same $J_{\pm\pm}<0$ case would not only lead to a coexistence of two domains from Fig. 13(d), but there are four distinct spin tilt angles in this case that need to be found numerically.

The saturation fields for the principal field directions can be straightforwardly found from vanishing of the high-field spectrum gap at the ordering vector at the transition [24, 25]. For the in-plane field directions for the Hamiltonian with the Zeeman term, taking $S=\frac{1}{2}$, this yields

$$h_s^{(b)} = g_{ab}\mu_B H_s^{(b)} = 4\Big(J_1+J_2-J_{\pm\pm}\Big), \qquad (3)$$
$$h_s^{(a)} = g_{ab}\mu_B H_s^{(a)} = 4\left(J_1+J_2-\frac{1}{2}J_{\pm\pm}\right),$$

note that $H_s^{(b)} > H_s^{(a)}$ since $J_{\pm\pm}<0$. For the stripe-**yz** case, one needs to switch the sign of $J_{\pm\pm}$ in (3) and $H_s^{(b)}$ with $H_s^{(a)}$.

Importantly, despite the uniform in-plane g-factor, the saturation fields are different for the two principal field directions, with the difference $\Delta h_s = 2|J_{\pm\pm}|$. This is a general consequence of the bond-dependent interactions in the anisotropic-exchange materials [23]. Note that the recent work on a different Ce-based triangular-lattice material, $KCeS_2$, has found a clear indication of the splitting of the transition lines in the H–T phase diagram for the two in-plane field directions [12], providing an evidence of the same trend.

Another important feature of Eq. (3) is that for the fixed J_2/J_1 only two parameters of the Hamiltonian define $H_s^{(a/b)}$, J_1 and $J_{\pm\pm}$, thus offering a strong constraint on them from the empirical value of the in-plane H_s. For the out-of-plane field, the saturation field is given by [24]

$$h_s^{(c)} = g_c\mu_B H_s^{(c)} = \Big(J_1+J_2\Big)\Big(3\bar{\Delta}+1\Big)+4|J_{\pm\pm}|, \quad (4)$$

that strongly depends on the XXZ anisotropy $\bar{\Delta}$.

To demonstrate the implications of these results, we complement them with the magnetization field-dependence $M(H)$ in the stripe-**x** phase at $T=0$ for the a- and b-directions in Fig. 14 and for the c-direction in Fig. 15, respectively. While for the b- and c-directions the spin tilting is simple and can be obtained analytically, for the a-direction the results are obtained from the numerical energy minimization. In all three directions, the stripe phase continuously deforms until reaching spin saturation at the corresponding critical field $H_s^{(a/b/c)}$ with no intermediate transitions.

The parameters that are used to obtain $M(H)$ in Fig. 14 and Fig. 15 are discussed in more detail below. At this stage it suffices to say that their choice is dic-

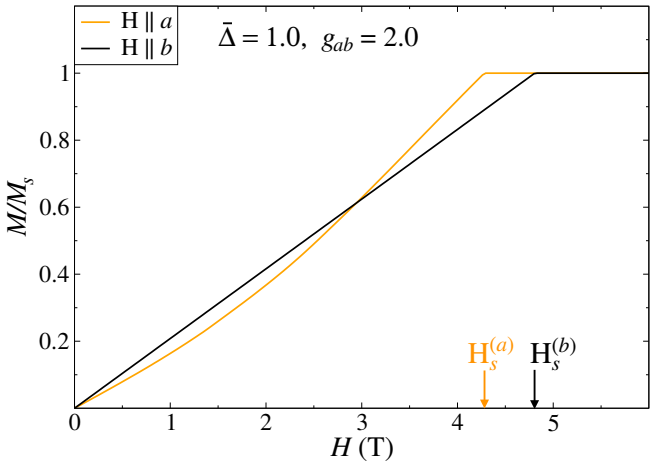

FIG. 14. The magnetization $M(H)$ in the stripe-**x** phase at $T=0$ for $H\parallel a$ and $H\parallel b$. Parameters of the Hamiltonian are to match $H_s^{exp}\approx 4.8$ T in the b-direction, and g-factors are as discussed in the text.

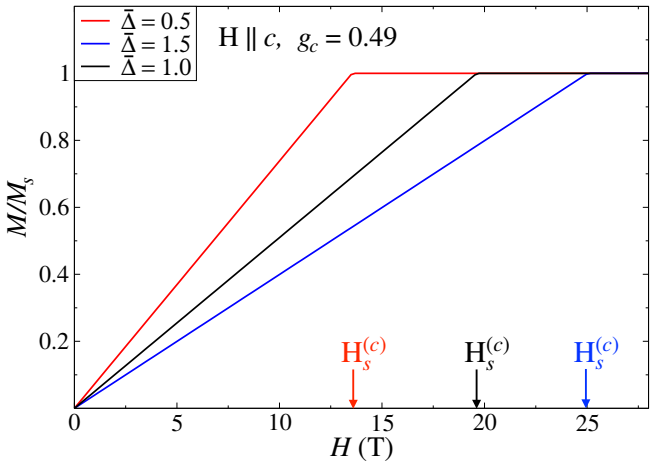

FIG. 15. Same as in Fig. 14 for $H\parallel c$ and for several $\bar{\Delta}$.

tated by matching experimental values of the zero-field gap and of the in-plane saturation field $H_s^{exp}\approx 4.8$ T, with the field assumed to be in the b-direction, and by varying the XXZ anisotropy $\bar{\Delta}$ in Fig. 15.

The difference of the saturation fields $H_s^{(b)}$ and $H_s^{(a)}$ in Fig. 14 is to be expected from the discussion following Eq. (3), with XXZ anisotropy having no bearing on the $M(H)$ curve for the field in the b-direction. Although $M(H)$ curves in Fig. 15 are featureless, the strong dependence of $H_s^{(c)}$ on $\bar{\Delta}$, also in accord with Eq. (4), is obvious. Unfortunately, the experimental restrictions on the actual value of the saturation field in the c-direction in $CeCd_3As_3$ are not tight enough, see [3]. While the value as low as 13 T as for $\bar{\Delta}=0.5$ is probably a stretch, it is difficult to narrow down the shown range of $\bar{\Delta}=0.5$–1.5 more significantly with the available data given possible uncertainties in the g-factors. The good news is that other quantities of interest that do depend on $\bar{\Delta}$ do so rather insignificantly, as we show below. Lastly, our choices of the g-factors differ somewhat from the results suggested in Ref. [3], $g_{ab}=2.0$ instead of 2.38 and $g_c=0.49$ instead of 0.46. These are to reflect slightly lower in-plane and higher out-of-plane initial slopes of $M(H)$ in the present study. A smaller g_{ab}-factor also seems to be supported by the value of the spin-excitation gap in the field 9 T, much above the saturation.

We add an extra note on the determination of $\bar{\Delta}$ parameter from the available data. The estimates on $\bar{\Delta}$ rely on the extrapolation of the magnetization vs field data for $H||c$, that do not reach $H_s^{(c)}$. There are two aspects of the extrapolation procedure for $H_s^{(c)}$ that are important. If one uses the data for $M(H)$ vs $H||c$ from Ref. [2], it would imply $H_s^{(c)}\approx 30$ T. The slope in our case, Fig. 2, is slightly higher, leading to an estimate of $H_s^{(c)}\approx 25$ T. However, both estimates are the subject of finite temperature effects, which suppress M vs H slope. For extracting model parameters such as $\bar{\Delta}$, we would ideally need $T=0$ data for $M(H)$. Although we cannot access it, we can estimate the effect of finite T ($\approx$2K) from the in-plane $M(H)$ results, for which finite-T $H_s^{(a/b)}$ is estimated as ≈ 7 T, while the low-T ("true") $H_s^{exp}\approx 4.8$ T, a $>30\%$ decrease. For the $H||c$ case, we take a conservative 20% reduction of the finite-T $H_s^{(c)}\approx 25$ T value to give the low-T $H_s^{(c)}\approx 20$ T. As one can see from our Fig.15, this yields $\bar{\Delta}$ very close to 1.0. The physically less motivated choices of $H_s^{(c)}\approx 13$ T gives $\bar{\Delta}=0.5$ and the extrapolated $H_s^{(c)}\approx 25$ T gives $\bar{\Delta}=1.5$. Thus, our choice of $\bar{\Delta}=1.0$ is well-justified.

D. Spin-wave theory

The spin-wave spectrum of the stripe phases in zero field and in fields above the saturation have been considered in the past [18, 24, 25]. Here we develop the linear spin-wave theory (LSWT) for the field-induced spin canted state in Fig. 13(b). The per-site classical energy is

$$\frac{E_{\rm cl}}{S^2}=\Big(J_1+J_2\Big)\Big(1-2\cos 2\varphi\Big)+2J_{\pm\pm}\Big(1+\cos 2\varphi\Big) - g_{ab}\mu_B H\sin\varphi/S, \quad (5)$$

with the canting angle φ. The energy minimization gives

$$\sin\varphi = H/H_s^{(b)}\equiv h, \quad (6)$$

see Eq. (3) for $H_s^{(b)}$.

Some straightforward algebra with the transformation of spins to a local reference frame and a Fourier transform give the LSWT Hamiltonian for $S=\frac{1}{2}$

$$\hat{\mathcal{H}}^{(2)}=\frac{3J_1}{2}\sum_{\mathbf{k}}\left(A_{\mathbf{k}}a^\dagger_{\mathbf{k}}a_{\mathbf{k}}-\frac{B_{\mathbf{k}}}{2}\left(a_{\mathbf{k}}a_{-\mathbf{k}}+\text{H.c.}\right)\right), \quad (7)$$

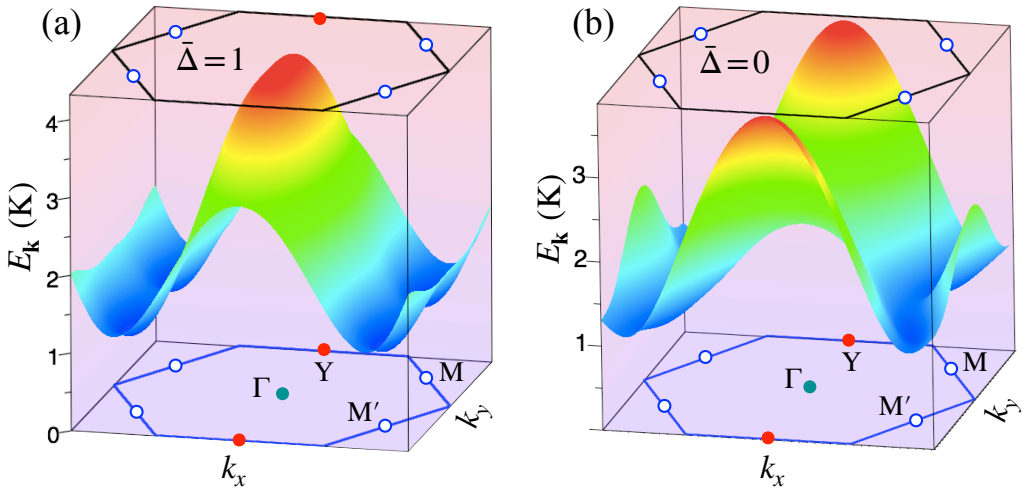

FIG. 16. The 3D plots of the $H=0$ magnon energy $\varepsilon_{\mathbf{k}}$ (in Kelvins) from Eq. (10) throughout the Brillouin zone for two representative sets of parameters. High-symmetry $\mathbf{k}$-points are indicated. The XXZ anisotropy is (a) $\bar{\Delta}=1$ and (b) $\bar{\Delta}=0$.

where $A_{\mathbf{k}}$ and $B_{\mathbf{k}}$ are given by

$$\begin{aligned} A_{\mathbf{k}} &= \frac{8}{3}(1+\alpha-\eta)h^2 + \frac{2}{3}(1+\alpha)(1-4h^2) - \frac{8}{3}(1-h^2)\eta \\ &+ \bar{\Delta}\gamma_{\mathbf{k}} + \bar{\gamma}_{\mathbf{k}} + h^2\left(\gamma_{\mathbf{k}} - \bar{\gamma}_{\mathbf{k}}\right) - 2\eta\left(\gamma'_{\mathbf{k}} - h^2\left(\gamma_{\mathbf{k}} + \bar{\gamma}_{\mathbf{k}}\right)\right) \\ &+ \alpha\left(\bar{\Delta}\gamma^{(2)}_{\mathbf{k}} + \bar{\gamma}^{(2)}_{\mathbf{k}} + h^2\left(\gamma^{(2)}_{\mathbf{k}} - \bar{\gamma}^{(2)}_{\mathbf{k}}\right)\right), \qquad (8) \\ B_{\mathbf{k}} &= -\bar{\Delta}\gamma_{\mathbf{k}} + \bar{\gamma}_{\mathbf{k}} + h^2\left(\gamma_{\mathbf{k}} - \bar{\gamma}_{\mathbf{k}}\right) - 2\eta\left(\gamma'_{\mathbf{k}} - h^2\left(\gamma_{\mathbf{k}} + \bar{\gamma}_{\mathbf{k}}\right)\right) \\ &+ \alpha\left(-\bar{\Delta}\gamma^{(2)}_{\mathbf{k}} + \bar{\gamma}^{(2)}_{\mathbf{k}} + h^2\left(\gamma^{(2)}_{\mathbf{k}} - \bar{\gamma}^{(2)}_{\mathbf{k}}\right)\right), \end{aligned}$$

where $\alpha = J_2/J_1$, $\eta = J_{\pm\pm}/J_1$, and

$$\begin{aligned} \gamma_{\mathbf{k}}\left[\bar{\gamma}_{\mathbf{k}}\right] &= \frac{1}{3}\left(\cos k_x \pm 2\cos\frac{k_x}{2}\cos\frac{\sqrt{3}k_y}{2}\right), \\ \gamma^{(2)}_{\mathbf{k}}\left[\bar{\gamma}^{(2)}_{\mathbf{k}}\right] &= \frac{1}{3}\left(\cos\sqrt{3}k_y \pm 2\cos\frac{3k_x}{2}\cos\frac{\sqrt{3}k_y}{2}\right), \qquad (9) \\ \gamma'_{\mathbf{k}} &= \frac{1}{3}\left(\cos k_x + \cos\frac{k_x}{2}\cos\frac{\sqrt{3}k_y}{2}\right). \end{aligned}$$

The standard Bogolyubov transformation of Eq. (7) yields the magnon energy for $0 \le H \le H_s^{(b)}$

$$\varepsilon_{\mathbf{k}} = \frac{3J_1}{2}\sqrt{A^2_{\mathbf{k}} - B^2_{\mathbf{k}}}\,. \qquad (10)$$

In Fig. 16, we show the 3D plots of the zero-field magnon energy $\varepsilon_{\mathbf{k}}$ in the stripe-$\mathbf{x}$ phase of Fig. 13(a), throughout the Brillouin zone, and for two representative sets of parameters that are chosen to match the experimental zero-field gap $\Delta^{exp}_{H=0} \approx 1$ K and the saturation field of $H_s^{exp} \approx 4.8$ T. The main message is that despite a rather drastic difference of the XXZ anisotropy parameter between Fig. 16(a) and Fig. 16(b), the minima of the spectrum are at the M and M′-points that are complementary to the ordering vector of the ground state, which is at the Y-point. In general, the structure of the low-energy part of the spectrum is rather robust to the parameter choices and consists of a quasi-degenerate region in $\mathbf{k}$-space connecting M and M′-points, see also Refs. [18, 24] for unrelated choices of parameters exhibiting the same pattern. The major difference between Fig. 16(a) and Fig. 16(b) is that the maximum of the magnon band migrates from the Γ-point to Y-point upon reducing $\bar{\Delta}$ from 1 to 0.

E. Gaps

From Eqs. (8) and (10), one can readily obtain the analytic expressions for the magnon energy gaps at the high-symmetry $\mathbf{k}$-points of interest

$$\begin{aligned} E_M &= E^0_M\sqrt{1+2h^2}\,, \quad \text{with} \\ E^0_M &= \sqrt{-2J_{\pm\pm}\left(-4J_{\pm\pm} + (J_1+J_2)\left(1-\bar{\Delta}\right)\right)}, \qquad (11) \\ E_Y &= E^0_Y\sqrt{1-h^2}\,, \quad \text{with} \\ E^0_Y &= \sqrt{h_s^{(b)}\left(-4J_{\pm\pm} + (J_1+J_2)\left(1-\bar{\Delta}\right)\right)}, \qquad (12) \end{aligned}$$

where $J_{\pm\pm} < 0$, $E^0_{M(Y)}$ are zero-field gaps, $h_s^{(b)}$ is from Eq. (3), and $h = H/H_s^{(b)}$. The "ordering gap" at the Y-point vanishes at the critical field for a transition to a paramagnetic state, as is expected. On the other hand, the "accidental gap" at the M-point, which is the spectrum minimum in zero field, increases with the field. Clearly, one should expect their crossing at some $H < H_s^{(b)}$.

F. Parameter sets

Before we proceed with the modeling of the $CeCd_3As_3$ spectrum, we need to specify parameters of the model that meet the phenomenological criteria for it. As is discussed above, we have already chosen $J_{z\pm} = 0$, fixed

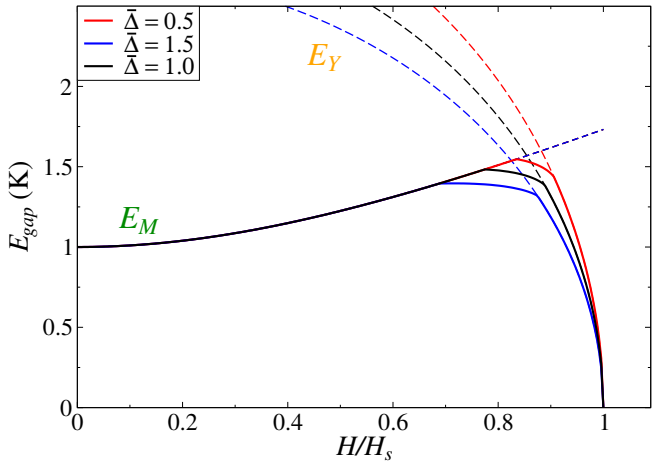

FIG. 17. Minimum of the spectrum $\varepsilon_{\mathbf{k}}$ (solid lines) and $E_{M(Y)}$ energies (dashed lines) vs H/H_s for the three parameter sets.

$J_2 = 0.1J_1$, and assumed $J_{\pm\pm} < 0$. For the remaining parameters, J_1, $\bar{\Delta}$, and $J_{\pm\pm}$, we have two strong constraints, the zero-field gap $\Delta^{exp}_{H=0} \approx 1$ K and the in-plane saturation field $H_s^{exp} \approx 4.8$ T, and one "soft" constraint for the out-of-plane saturation field $H_s^{(c)}$ to be within 15–30 T window.

Since the theoretical value for $H_s^{(c)}$ is the only quantity that strongly depends on $\bar{\Delta}$, we use the latter constraint to provide us with the broad bounds it. Then, we choose several reasonable values of $\bar{\Delta}$ and use the two strong criteria to fix J_1 and $J_{\pm\pm}$.

Roughly speaking, the zero-field gap at the M-point from Eq. (11) fixes $J_{\pm\pm}$ and the in-plane saturation field $H_s^{(b)}$ from Eq. (3) fixes J_1. Neglecting $J_{\pm\pm}$ from Eq. (3) and setting $\bar{\Delta} = 1$ in Eq. (11) yield the estimates $J_1 \approx 1.5$ K and $J_{\pm\pm} \approx 0.35$ K. More precise calculations, using $E_M^0 = \Delta^{exp}_{H=0}$ with Eq. (11), $H_s^{(b)} = H_s^{exp}$ with Eq. (3), and the in-plane g-factors $g_{ab} = 2.0$ and $g_c = 0.49$ as discussed above, produce three representative sets

$\bar{\Delta}$	J_1	$J_{\pm\pm}$	$H_s^{(c)}$
0.5	1.21 K	-0.280 K	13.0 T
1.0	1.14 K	-0.354 K	19.0 T
1.5	1.07 K	-0.435 K	24.6 T

which we will refer to by their respective choices of the XXZ anisotropy parameter $\bar{\Delta}$ in the first column. The last column shows the out-of-plane saturation field $H_s^{(c)}$ that corresponds to each set, giving a sense that the choices of $\bar{\Delta} = 0.5$ and $\bar{\Delta} = 1.5$ are likely to be outliers and $\bar{\Delta} = 1$ is a reasonable choice.

G. Gap vs field results

We are now set to study the spectral properties of $CeCd_3As_3$. Our Fig. 17 shows the field dependence of the spectrum minimum for the three parameter sets introduced above; the energies are in K and the field is in units of $H_s^{(b)}$. The solid line traces the true "minimal gap" of the spectrum $\varepsilon_{\mathbf{k}}$ in Eq. (10), while the dashed lines track the energies of the M and Y-points, Eqs. (11) and (12), respectively. The dashed curves intersect below H_s, as anticipated. The overall behavior of the minimal gap is notable: a gradual increase followed by a rather abrupt transition to a steep decrease and closing at the critical point, with the results that only moderately depend on the XXZ anisotropy in the allowed range.

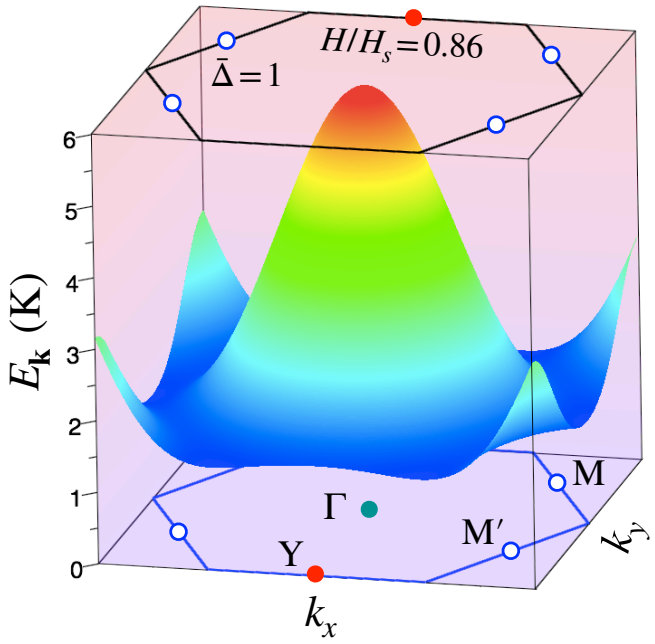

FIG. 18. $\varepsilon_{\mathbf{k}}$ at $H = 0.86H_s$ for the $\bar{\Delta} = 1$ parameter set.

The true minimal gap in Fig. 17 has some field region where it is neither at M nor at Y-point, but at the $\mathbf{k}$-points that are intermediate between them, the situation that is illustrated in Fig. 18 for the field $H = 0.86H_s$ and for the $\bar{\Delta} = 1$ parameter set, for which the spectrum minimum is nearly degenerate along a contour that includes M, M′, and Y-points.

A complementary prospective is also offered by the magnon density of states (DoS) in Fig. 19, the quantity that is directly related to the specific heat. This figure explicitly shows the field-induced spectral weight redistribution due to the gap crossing and Van Hove singularities associated with the spectrum degeneracies. It suggests that the higher density of states may lead to additional features in the specific heat.

H. Polarized phase

Above the saturation field, spins' quantization axis aligns with the field direction and the spin-wave algebra simplifies considerably [24, 25]. For the field $H \geq H_s^{(b)}$ in the b-direction, the $A_{\mathbf{k}}$ and $B_{\mathbf{k}}$ terms in the LSWT

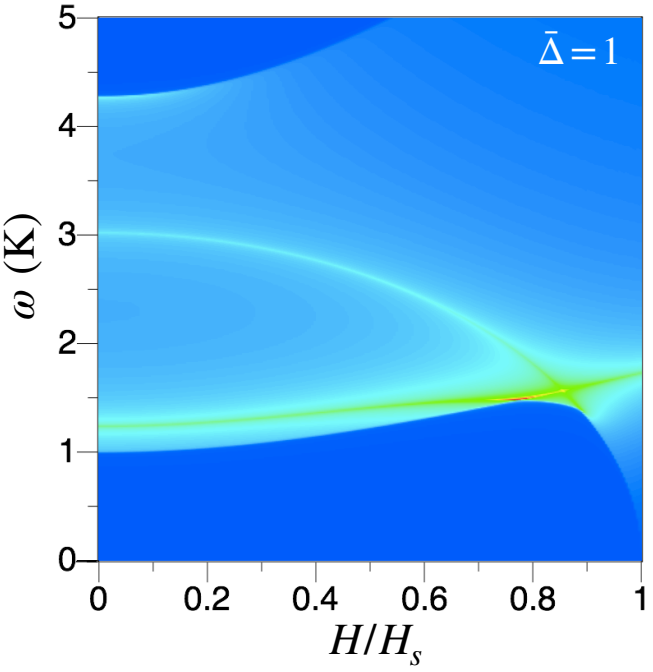

FIG. 19. Magnon DoS vs H/H_s for the $\bar{\Delta}=1$ parameter set.

Hamiltonian (7) are given by

$$\widetilde{A}_{\mathbf{k}} = \frac{8}{3}(1+\alpha-\eta)h - 2(1+\alpha) + (1+\bar{\Delta})\left(\gamma_{\mathbf{k}} + \alpha\gamma_{\mathbf{k}}^{(2)}\right) + 2\eta\gamma''_{\mathbf{k}}, \qquad (13)$$
$$\widetilde{B}_{\mathbf{k}} = (1-\bar{\Delta})\left(\gamma_{\mathbf{k}} + \alpha\gamma_{\mathbf{k}}^{(2)}\right) + 2\eta\gamma''_{\mathbf{k}},$$

where $\alpha = J_2/J_1$, $\eta = J_{\pm\pm}/J_1$, $h = H/H_s^{(b)}$ as before, $\gamma_{\mathbf{k}}$ and $\gamma_{\mathbf{k}}^{(2)}$ given in Eq. (9) and

$$\gamma''_{\mathbf{k}} = \frac{1}{3}\left(\cos k_x - \cos\frac{k_x}{2}\cos\frac{\sqrt{3}k_y}{2}\right). \qquad (14)$$

We note that in the case of $H \parallel a$ the expression is the same up to the change $J_{\pm\pm} \to -J_{\pm\pm}$.

The energy spectrum has the same form as in (10)

$$\varepsilon_{\mathbf{k}} = \frac{3J_1}{2}\sqrt{\widetilde{A}_{\mathbf{k}}^2 - \widetilde{B}_{\mathbf{k}}^2}\,. \qquad (15)$$

At the saturation field, Eqs. (10) and (15) yield the same result. The spectrum has a gapless mode at the Y-point that has an acoustic character, i.e., $\varepsilon_{\mathbf{k}} \propto |\delta\mathbf{k}|$, where $\delta\mathbf{k} = \mathbf{k} - \mathbf{k}_Y$. This is the behavior that is generally expected for the transitions in anisotropic systems, see more discussion in Sec. VIII.

Above the saturation field, the gap at the Y-point reopens, but the spectrum does not experience any significant transformations aside from a roughly uniform, Zeeman-like shift of the spectrum as a whole. That is, the Y-point remains a minimum for all $H \geq H_s^{(b)}$ with

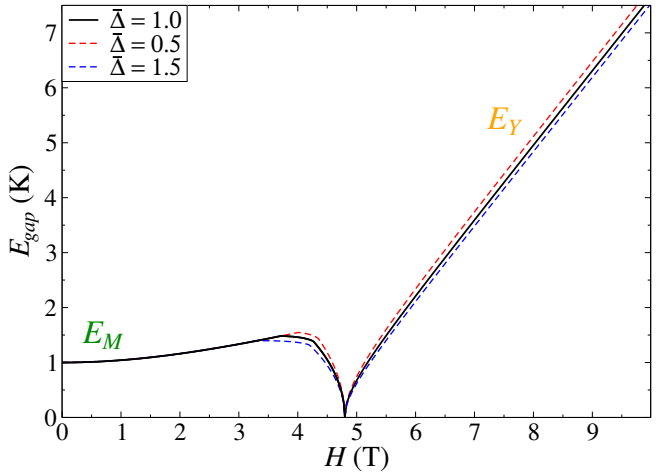

FIG. 20. Minimum of the spectrum $\varepsilon_{\mathbf{k}}$ vs H for the three parameter sets, and $g_{ab}=2.0$.

the gap

$$\widetilde{E}_Y = \sqrt{\left(\widetilde{h} - h_s^{(b)}\right)\left(\widetilde{h} - (J_1+J_2)\left(3+\bar{\Delta}\right)\right)}, \qquad (16)$$

where $h_s^{(b)}$ is from Eq. (3) and $\widetilde{h} = g_{ab}\mu_B H$.

In Fig. 20, we present the field-dependence of the spectrum minimum in both regions, $H \leq H_s^{(b)}$ and $H \geq H_s^{(b)}$, for the three parameter sets and g_{ab} discussed above.

Our Fig. 21 reproduces Fig. 3 of the main text on the linear scale. It shows the "minimal gap" together with the gaps at the M- and Y-points throughout the entire field regime for the $\bar{\Delta}=1$ parameter set and together with experimental data. We point out again that after $\bar{\Delta}$ and J_2/J_1 are fixed, the remaining parameters of the model, J_1 and $J_{\pm\pm}$, are fully constrained by the saturation field value H_s^{exp} and the zero-field gap $E_{gap}^{exp}(H=0)$. There are no free parameters left. Yet the theoretical curve goes right through the value of the gap at 9 T with no fitting.

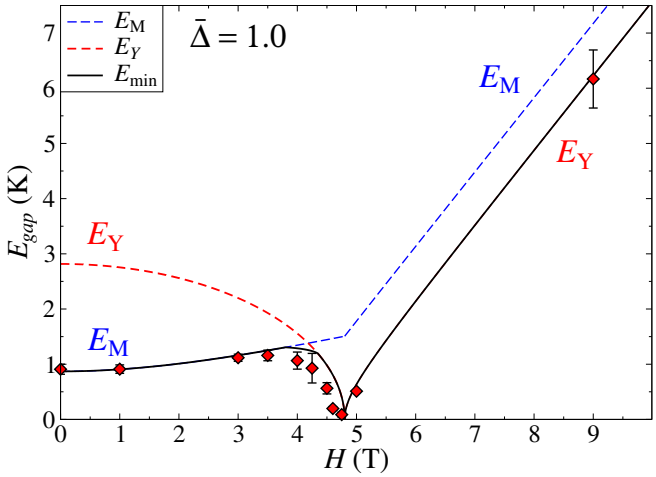

FIG. 21. Fig. 3 of the main text on the linear scale.

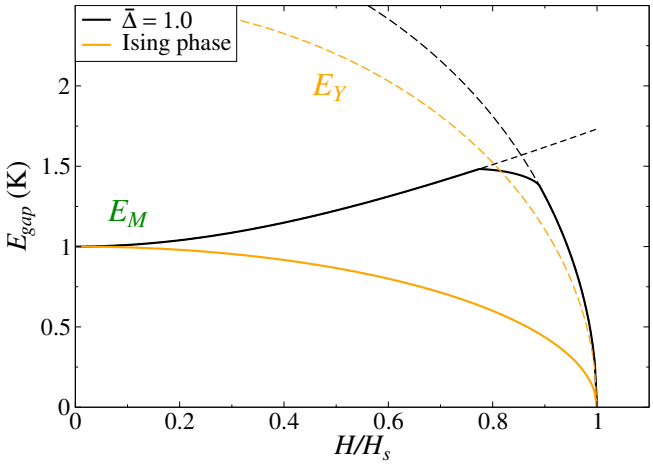

FIG. 22. Same as Fig. 17 for the Ising-like stripe-**z** phase.

I. Ising phase gaps

As was discussed earlier, the only feasible alternative to the gapped stripe state is an Ising-like state that does not need bond-dependent terms at all. However, on a triangular lattice, the simplest candidate, the nearest-neighbor-only phase, is a gapless and ferrimagnetic. It is a relative of the 120° phase with the plane containing the triad of spins turned perpendicular to the basal plane and spins forming a deformed "Y" structure with a net magnetic moment [19].

The gapped state is reached with the help of a finite J_2 and is a stripe-like phase with spins pointing along the z-axis, referred to as a stripe-**z** phase. It is known to exhibit a staircase of the spin-flop transitions starting at low fields in the c-direction [20], the features that are not observed in the $M(H)$ data $CeCd_3As_3$.

Nevertheless, we have volunteered to provide a study of the field-dependence of the spectrum gap in this phase for the in-plane field. Our Fig. 22 shows the the excitation energies of the "accidental" and "ordering" M and Y-points for a representative parameter set from this phase: $J_1 = 1.13$ K, $J_2 = 0.2J_1$, $J_{\pm\pm} = 0$, and $\bar{\Delta} = 1.735$. This set of parameters matches the zero-field gap value of 1 K and the saturation field value of 4.8 T with the same g-factor as before. Having $J_{\pm\pm} \neq 0$ does not change the field-dependence of the gaps in the stripe-**z** phase in any quantitative way. These results are also compared to the ones for the $\bar{\Delta} = 1.0$ stripe-**x** parameter set from Fig. 17.

One can see a markedly different behavior of the gaps in the stripe-**z** phase. The gap at the M-point remains an absolute minimum of the spectrum for the entire field range, is monotonically decreasing vs field, and vanishes at the critical point together with the gap at the ordering vector (Y-point). This is because for the stripe-**z** state at the full polarization point, all three stripe domains of different orientation are degenerate. There is no level-crossing in the spectrum and no abrupt change in the minimal gap behavior vs field. Needless to say, this is inconsistent with the $CeCd_3As_3$ phenomenology.

VII. NÉEL TEMPERATURE

We have modified the so-called self-consistent random-phase approximation (RPA) to calculate Néel ordering temperature and its field-dependence for the selected parameter sets for the stripe state. The self-consistent RPA approach is based on the mean-field decoupling of the equations of motion for the spin Green's functions and has been recently employed in the context of the anisotropic-exchange systems, see Refs. [18, 23] for details.

In our case, the RPA approach for the ordering temperature T_N needed to be modified to account for the order parameter corresponding to the component of the ordered moment that is transverse to the external field. The result is particularly simple

$$\frac{1}{T_N} = \frac{3J_1 \cos\varphi}{N} \sum_{\mu,\mathbf{k}} \frac{A_{\mathbf{k}}}{\varepsilon^2_{\mathbf{k}}}, \tag{17}$$

where φ is the spin canting angle in Fig. 13(b).

Our Fig. 23 presents the results of such calculations. The overall shape of the H–T phase diagram is in a general accord with the data for $CeCd_3As_3$. However, there are two significant differences. While the RPA method offers a significant improvement over the "bare" mean-field values [18], the absolute values of T_N are still at least a factor of two larger than in the experiment. The second crucial difference is the lack of the notable initial increase in the T_N vs field in the RPA results compared with the experimental data, with the latter suggesting a linear slope, $\delta T_N \propto |H|$. The observations in a different Ce-based compound also indicate a similar increase [12].

Both discrepancies are of the same origin. The quantitative successes and failures of the RPA method are known [26], but the reason for them is not properly discussed. The key issue is that this method is based on the

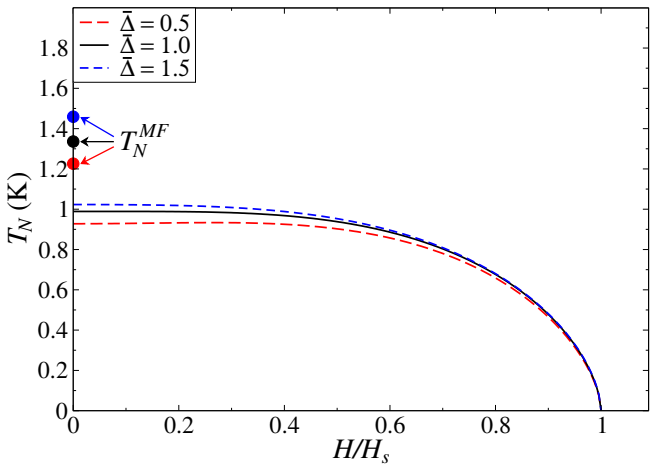

FIG. 23. T_N vs field by the self-consistent RPA approach for the three parameter sets. Mean-field (MF) results for zero field are shown for comparison.

picture of thermal reduction of the local order parameter and, thus, is just a glorified Lindemann criterion for melting of a given spin order. It is quite successful quantitatively in the 2D systems with continuous symmetries, in which the ordering happens when the 2D correlation length is very large and the fluctuating component into the 3D ordering is small. For all other cases, since it does not include critical fluctuations into consideration, it fails. We can also state that since the RPA results for T_N (17) are based on the spectrum $\varepsilon_{\mathbf{k}}$ from Eq. (10), they can only contain terms $\propto H^2$, but not the linear term. Therefore, the origin of the latter is most likely in the field-induced suppression of the critical fluctuations. At larger fields, the order parameter reduction due to spin canting dominates and the agreement improves.

VIII. SPECIFIC HEAT AND VARIOUS ASYMPTOTES

At low temperatures, population of spin excitations is low and can be approximated by a bosonic statistics. This is also a description of such excitations within the spin-wave approach. Then, the specific heat is given by

$$C(T) = \frac{\partial E}{\partial T} = \sum_{\mathbf{k}} \left(\frac{\varepsilon_{\mathbf{k}}}{T}\right)^2 \frac{e^{\varepsilon_{\mathbf{k}}/T}}{(e^{\varepsilon_{\mathbf{k}}/T}-1)^2} \ . \qquad (18)$$

The results obviously depend on the spectrum $\varepsilon_{\mathbf{k}}$ and on the dimensionality of the system. We use this expression to obtain the leading, asymptotically correct terms in the specific heat T-dependence in 2D for both gapped and gapless spectra at low temperatures. Since the results are expected to be generic, the Debye approximation, that uses the low-energy form of the spectrum and a cut-off Debye momentum, suffices.

A. Gapped spectrum

For the gapped spectrum near the minimum, spin-excitation energy can be approximated as

$$\varepsilon_{\mathbf{k}} \approx \Delta + J\mathbf{k}^2 \ , \qquad (19)$$

with the "kinetic" energy that can be related to the bandwidth $W = Jk_D^2$, where k_D is the Debye momentum. In 2D, this yields $C(T)$ in the Debye approximation

$$C(T) = \frac{T}{W}\int_{x_0}^{x_m} dx\ x^2\ \frac{e^x}{(e^x-1)^2} \ , \qquad (20)$$

where $x_0 = \Delta/T$ and $x_m = x_0 + W/T$. In the limit $T \ll \Delta$, $T \ll W$, a simple algebra gives

$$C(T) \approx \frac{T}{W}\left(\frac{\Delta^2}{T^2} + \frac{2\Delta}{T} + 2\right) e^{-\Delta/T} \qquad (21)$$

with the omitted terms of order $O\left(e^{-2\Delta/T}; e^{-\Delta/T - W/T}\right)$.

A different, "relativistic" form of the gapped spectrum can be of interest, especially close to the critical field

$$\varepsilon_{\mathbf{k}} \approx \sqrt{\Delta^2 + J^2\mathbf{k}^2} \ . \qquad (22)$$

Following the same steps as above results in

$$C(T) \approx AT\left(\frac{\Delta^2}{T^2} + \frac{3\Delta}{T} + 6 + \frac{6T}{\Delta}\right) e^{-\Delta/T} \qquad (23)$$

with the leading term coinciding with the one in Eq. (21), both corresponding to an activated behavior of the specific heat with the leading T^{-d+1} prefactor. These expressions allow to extract the value of the lowest gap in the spectrum from the activated behavior of $C(T)$.

B. Gapless spectrum at the critical point

The field-induced transitions of an antiferromagnet to a saturated, paramagnetic state are common. For the systems with the continuous spin symmetries, the magnetic field coupling is to a conserved total magnetization and the transition is of the Bose-Einstein condensation type [27, 28]. In this case, the dispersion relation of the bosonic excitations at the QCP is $\varepsilon_{\mathbf{k}} \propto \mathbf{k}^2$ (dynamical exponent $z=2$). Above the saturation field the spectrum is Zeeman-shifted, but otherwise unmodified.

In our case, because of the symmetry-breaking anisotropic terms, magnetization is not a conserved quantity and the transition is of a different universality class, necessarily resulting in an acoustic-like $\varepsilon_{\mathbf{k}} \propto |\mathbf{k}|$ (dynamical exponent $z=1$), see Ref. [28]. Following the derivation that is analogous to the textbook one for phonons, the leading term in the specific heat is a power law

$$C(T) \approx AT^2 \qquad (24)$$

with the power $d=2$ and A is a constant.

Tracking the field-dependent specific heat should allow to identify the field value that yields such a behavior at low temperatures. In practice, it may be difficult to locate such a point exactly, so a different "double asymptotic" expansion may be useful. One needs to consider specific heat (18) for the relativistic dispersion of Eq. (22) in the limit of $T \gg \Delta$, but still $T \ll W$. A straightforward algebra yields a gap-dependent correction to (24)

$$C(T) \approx AT^2\left(1 - \frac{\Delta^2}{\alpha T^2}\right) \qquad (25)$$

where $\alpha = 12\zeta(3)$ with $\zeta(3) \approx 1.2$. This approximation should be valid down to $T \sim \Delta/2$.

In the main text we presented specific heat data for $CeCd_3As_3$ for two fields near the QCP and their fits using the asymptotic expressions of Eqs. (25) and (24). The fits suggest that the 4.75 T field is at or very close to the QCP as it is well-fit by the T^2 power-law, while the 4.6 T low-temperature data are well-fit by the asymptote

in Eq. (25) with a small gap of $\Delta = 0.16$ K. We would like to point out that the success of these fits may be fortuitous as the "real" LSWT dispersions from Eq. (10) also contain the non-linear terms that can affect the asymptotic behavior in this temperature regime.

C. Other anomalies in the specific heat

In the $CeCd_3As_3$, in the field region between ~ 4 T and 4.6 T approaching the QCP, specific heat data demonstrates additional feature besides the one that is associated with the proper phase transition, potentially suggesting a sliver of another phase.

As was discussed in Sec. VI G, one possible scenario of the origin of this feature is in the transformation of the spin-excitation spectrum, which occurs in a similar field range and is responsible for additional Van Hove singularities that may contribute to the specific heat. Unfortunately, the characteristic temperatures of these features are such that the bosonic approximation for the specific heat may be unreliable. We, therefore, cannot substantiate this scenario as unbiased numerical methods are needed. We point out that some frustrated models on the triangular lattice consistently demonstrate a two-peak structure in their specific heat for some parts of the phase diagram as obtained by exact diagonalization [29]. Their origin may be related to the one suggested above.

The second scenario involves real-life complications. The difference of the critical fields in the a and b directions in Eq. (3) and in Fig. 14 translates into $\Delta H_s \lesssim 0.5$ T for the realistic parameters that we study. This is about the same as the width of the suggested additional phase in the H–T phase diagram of $CeCd_3As_3$. Thus, one cannot exclude that the additional features are associated with different transition temperatures in different stripe domains of the type discussed in Sec. VI B and shown in Fig. 13, which survive because of pinning by disorder. Within this scenario, it needs to be explained, though, why they do not show up at the lower fields.

Lastly, another rare-earth triangular-lattice material, $YbMgGaO_4$, has also been suggested to belong to a stripe phase, which, however, is "molten" by an inter-site mixing of the non-magnetic Mg and Ga ions that affects magnetism in Yb^{+3} layers, leading to a spin-liquid "mimicry" [24]. The key differences of $CeCd_3As_3$ and its stripe phase are the following. First, there is no Cd/As site-mixing in the case of $CeCd_3As_3$, only a partial occupation of sites, with the latter not changing the triangular symmetry at Ce sites, see Fig. 1. The second important difference is that the proposed stripe-phase in $YbMgGaO_4$ is nearly gapless and belongs to a different region of the phase diagram in a close proximity of the 120° region. This is also corroborated by an indication of plateau-like transitions in external field [30]. In case of $CeCd_3As_3$, a strong gap "protects" from randomization of exchange parameters. This may also make a disorder relevant to the appearance of the "intermediate" phase upon suppression of the gap with the field.

[1] S. S. Stoyko and A. Mar, Ternary Rare-Earth Arsenides $REZn_3As_3$(RE=La-Nd, Sm) and $RECd_3As_3$(RE=La-Pr), Inorg. Chem. **50**, 11152 (2011).

[2] Y. Q. Liu, S. J. Zhang, J. L. Lv, S. K. Su, T. Dong, G. Chen, and N. L. Wang, Revealing a Triangular Lattice Ising Antiferromagnet in a Single-Crystal $CeCd_3As_3$ (2016), arXiv:1612.03720.

[3] J. Banda, B. K. Rai, H. Rosner, E. Morosan, C. Geibel, and M. Brando, Crystalline Electric Field of Ce in Trigonal Symmetry: $CeIr_3Ge_7$ as a Model Case, Phys. Rev. B **98**, 195120 (2018).

[4] P. Pagliuso, D. Garcia, E. Miranda, E. Granado, R. Serrano, C. Giles, J. Duque, R. Urbano, C. Rettori, J. Thompson, M. Hundley, and J. Sarro, Evolution of the Magnetic Properties and Magnetic Structures Along the R_mMIn_{3m+2} (R=Ce, Nd, Gd, Tb; M=Rh, Ir; and m=1,2) Series of Intermetallic Compounds, J. Appl. Phys. **99**, 08P703 (2006).

[5] A. Scheie, V. O. Garlea, L. D. Sanjeewa, J. Xing, and A. S. Sefat, Crystal Field Hamiltonian and Anisotropy in $KErSe_2$ and $CsErSe_2$, Phys. Rev. B **101**, 144432 (2020).

[6] S. R. Dunsiger, J. Lee, J. E. Sonier, and E. D. Mun, Long-Range Magnetic Order in the Anisotropic Triangular Lattice System $CeCd_3As_3$, Phys. Rev. B **102**, 064405 (2020).

[7] E. Gopal, *Specific Heats at Low Temperatures*, The International Cryogenics Monograph Series (Springer US, 1966).

[8] Y. T. Fan, W. H. Lee, and Y. Y. Chen, Antiferromagnetic Spin Wave in Ce_2PdGe_6, Phys. Rev. B **69**, 132401 (2004).

[9] W. P. Halperin, F. Rasmussen, C. Archie, and R. Richardson, Properties of Melting ^{3}He: Specific Heat, Entropy, Latent Heat, and Temperature, J. Low Temp. Phys. **31**, 617 (1978).

[10] J. Lee, A. Rabus, N. Lee-Hone, D. Broun, and E. Mun, The Two-Dimensional Metallic Triangular Lattice Antiferromagnet $CeCd_3P_3$, Phys. Rev. B **99**, 245159 (2019).

[11] S. Higuchi, Y. Noshima, N. Shirakawa, M. Tsubota, and J. Kitagawa, Optical, Transport and Magnetic Properties of New Compound $CeCd_3P_3$, Mat. Res. Exp. **3**, 056101 (2016).

[12] G. Bastien, B. Rubrecht, E. Haeussler, P. Schlender, Z. Zangeneh, S. Avdoshenko, R. Sarkar, A. Alfonsov, S. Luther, Y. A. Onykiienko, H. C. Walker, H. Kuhne, V. Grinenko, Z. Guguchia, V. Kataev, H.-H. Klauss, L. Hozoi, J. van den Brink, D. S. Inosov, B. Buchner, A. U. B. Wolter, and T. Doert, Long-Range Magnetic Order in the $\tilde{S} = 1/2$ Triangular Lattice Antiferromagnet $KCeS_2$, SciPost Phys. **9**, 041 (2020).

[13] N. Kabeya, T. Sakamoto, K. Hara, Y. Hara, S. Nakamura, K. Katoh, and A. Ochiai, Competing Exchange Interactions in Lanthanide Triangular Lattice Compounds $LnZn_3P_3$ (Ln=La-Nd, Sm, Gd), J. Phys. Soc. Japan **89**,

074707 (2020).
[14] Y. D. Li, X. Wang, and G. Chen, Anisotropic Spin Model of Strong Spin-Orbit-Coupled Triangular Antiferromagnets, Phys. Rev. B **94**, 035107 (2016).
[15] J. A. M. Paddison, M. Daum, Z. Dun, G. Ehlers, Y. Liu, M. B. Stone, H. Zhou, and M. Mourigal, Continuous Excitations of the Triangular-Lattice Quantum Spin Liquid $YbMgGaO_4$, Nature Phys. **13**, 117 (2017).
[16] Z. Zhu, P. Maksimov, S. White, and A. Chernyshev, Topography of Spin Liquids on a Traingular Lattice, Phys. Rev. Lett. **120**, 207203 (2018).
[17] Y. Li, G. Chen, W. Tong, L. Pi, J. Liu, Z. Yang, X. Wang, and Q. Zhang, Rare-Earth Triangular Lattice Spin Liquid: A Single-Crystal Study of $YbMgGaO_4$, Phys. Rev. Lett. **115**, 167203 (2015).
[18] P. A. Maksimov, Z. Zhu, S. R. White, and A. L. Chernyshev, Anisotropic-Exchange Magnets on a Triangular Lattice: Spin Waves, Accidental Degeneracies, and Dual Spin Liquids, Phys. Rev. X **9**, 021017 (2019).
[19] S. Miyashita, Magnetic Properties of Ising-Like Heisenberg Antiferromagnets on the Triangular Lattice, J. Phys. Soc. Japan **55**, 3605 (1986).
[20] L. Seabra and N. Shannon, Competition Between Supersolid Phases and Magnetization Plateaus in the Frustrated Easy-Axis Antiferromagnet on a Triangular Lattice, Phys. Rev. B **83**, 134412 (2011).
[21] O. A. Starykh, Unusual Ordered Phases of Highly Frustrated Magnets: a Review, Rep. Prog. Phys. **78**, 052502 (2015).
[22] J. G. Rau, P. A. McClarty, and R. Moessner, Pseudo-Goldstone Gaps and Order-by-Quantum-Disorder in Frustrated Magnets, Phys. Rev. Lett. **121**, 237201 (2018).
[23] P. A. Maksimov and A. L. Chernyshev, Rethinking α-$RuCl_3$, Phys. Rev. Research **2**, 033011 (2020).
[24] Z. Zhu, P. Maksimov, S. White, and A. Chernyshev, Disorder-Induced Mimicry of a Spin Liquid in $YbMgGaO_4$, Phys. Rev. Lett. **119**, 157201 (2017).
[25] Y. D. Li, Y. Shen, Y. Li, J. Zhao, and G. Chen, Effect of Spin-Orbit Coupling on the Effective-Spin Correlation in $YbMgGaO_4$, Phys. Rev. B **97**, 125105 (2018).
[26] E. V. Komleva, V. Y. Irkhin, I. V. Solovyev, M. I. Katsnelson, and S. V. Streltsov, Unconventional Magnetism and Electronic State in Frustrated Layered System $PdCrO_2$, Phys. Rev. B **102**, 174438 (2020).
[27] E. G. Batyev and L. S. Braginskii, Antiferrormagnet in a Strong Magnetic Field: Analogy with Bose Gas, Sov. Phys. JETP **60**, 781 (1984).
[28] V. Zapf, M. Jamie, and C. D. Batista, Bose-Einstein Condensation in Quantum Magnets, Rev. Mod. Phys. **86**, 563 (2014).
[29] B. Schmidt and P. Thalmeier, Frustrated Two Dimensional Quantum Magnets, Phys. Rep. **703**, 1 (2017).
[30] W. M. Steinhardt, Z. Shi, A. Samarakoon, S. Dissanayake, D. Graf, Y. Liu, W. Zhu, C. Marjerrison, C. D. Batista, and S. Haravifard, Contraining the Parameter Space of a Quantum Spin Liquid Candidate in Applied Field with Iterative Optimization (2020), arXiv:1902.07825.